

Tissue can generate propagating long-range forces on weakly adhesive substrate

Yuting Lou,^{1,*} Takumi Kawaue,¹ Ivan Yow,¹ Yusuke Toyama,¹ Jacques Prost,^{1,2} and Tetsuya Hiraiwa^{1,†}

¹*Mechanobiology Institute, National University of Singapore, Singapore 117411, Singapore*

²*Laboratoire Physico Chimie Curie, Institut Curie, Paris Science et Lettres Research University, CNRS UMR168, 75005 Paris, France*

(Dated: August 23, 2022)

Cells in a tissue mutually coordinate their behaviors to maintain tissue homeostasis and control morphogenetic dynamics. As well as chemical signals, mechanical entities such as force and strain can be possible mediators of the signalling cues for this mutual coordination, but how such mechanical cues can propagate has not been fully understood. Here, we propose a mechanism of long-range force propagation through the extracellular matrix. We experimentally found a novel concentric wave of deformation in the elastic substrate underlying an epithelial monolayer around an extruding cell, under weakly-adhesive conditions which we define in our work. The deformation wave propagates over two cell sizes in ten minutes. The force transmission is revealed by the emergence of a pronounced peak in the deformation field of substrate. We derive a theoretical model based on linear elasticity theory, to analyse the substrate dynamics and to quantitatively validate this model. Through model analysis, we show that this propagation appears as a consequence of the stress exerted by the tissue on a soft substrate sliding on a stiff one. These results infer that the tissue can interact with embedding substrate with weakly adhesive structures to precisely transmit long-range forces for the regulation of a variety of cellular behaviors.

* chelinqueen@hotmail.com

† mbithi@nus.edu.sg

I. INTRODUCTION

It is now widely accepted that mechanics is a key player for understanding how cells coordinate tissue morphodynamics and homeostasis. Cells can sense the mechanical stress or strain in a tissue or in the environment, which can regulate cell migration and spreading, cell division rate and differentiation [1–8]. Simultaneously, cells can generate mechanical stresses and forces in a tissue. Earlier works revealed multiple ways in which forces originate in *in situ* biological systems, like anisotropic and pulsed actomyosin contractions [9–11] and apoptotic forces [12, 13], and the relevance for the morphogenetic dynamics. Such mechanical stresses or forces generated by cells in a tissue can function as a mechanical cue for the autonomous coordination of cellular behaviors within the tissue. For example, the spatiotemporal pattern of intercellular forces in a tissue can steer collective cell migration for wound healing [14–19]. Cell cycle progression is also regulated by intercellular force [20], suggesting that the force may be relevant for maintaining tissue homeostasis.

One of the important factors which can influence such autonomous coordination by a mechanical cue may be the way the mechanical stress or the force exerted by a cell is transmitted to other cells. Extracellular matrix (ECM), as well as cells themselves, may work as an important mediator of mechanical cues. The mechanical response of ECM to the force exerted by cells has been studied for certain situations. For instance, several groups have addressed how deeply cells can feel ECM, both experimentally using various thickness of substrates and theoretically solving the elastic substrate model [21–24]. These studies assumed the simplest situation, in which the bottom of the substrate underlying the tissue strongly adheres to another rigid base so that the substrate cannot move. Owing to this immobility, the deformation of a substrate is constrained by the substrate thickness and therefore the stress cannot propagate farther than the scale of the thickness. However, in a multicellular organism, it is likely that tissues are not always strongly bonded to some rigid ECM structures because of the complexity in ECM constitutions as well as remodeling mechanisms, which may allow ECM to mediate forces at long distances. This force propagation through ECM remains overlooked in the studies of cell-ECM interactions and so far no experiment has been developed to study this aspect in a controlled way.

In this article, we aim to study the role of ECM in transmitting long-range forces in tissues. We approach this issue by focusing ourselves on a simplified three-layered system, where a tissue layer locates on a elastic substrate which weakly adheres to another base. Our new findings are based on the following experimental results. We induced an apoptotic event in a epithelial monolayer on a gel with weakly adhesive interface to a glass base [Fig. 1 (A)] and observed a well-defined concentric propagation of gel deformation over a distance longer than a typical cell diameter around the cell undergoing extrusion process [Fig. 1(B, C)]. To study the physical mechanisms underlying this novel form of long-range propagation, we decided to focus on the mechanical aspects of the system. This point of view comes from the consideration of the following facts. On one hand, chemical waves like calcium waves[25] observed in cell extrusion experiments manifest over a scale of seconds after cell extrusion, which makes them highly unlikely to account for the hour-long scale concentric wave observed in our experiments; on the other hand, mechanical forces govern the cell extrusion process for a period of 40 minutes [26] after the ablation, which is more relevant to the time scale of our interest. Indeed, biochemical processes can be coupled on this hour-scale due to the tissue responses to apoptosis; hence, we decouple the tissue responses from the gel mechanics in a model and analyze the gel deformation dynamics under various assumptions of tissue processes as an external force source exerted to the gel surface.

Based on this view, we applied an elastic gel theory to this system [Fig. 1(D)] and revealed that the competition between the simple linear elasticity of a gel and gel-glass friction can quantitatively reproduce this long-range propagation of gel deformation as observed in our experiments. We also experimentally and theoretically demonstrated that a rigid gel-glass interface is incapable of reproducing this sharp deformation peak or the observed propagation dynamics. These results suggest that the weakly adhesive structures of substrates, especially those lacking elastic restoration force against layerwise shearing, play a role in mediating a mechanical cue over long distances. Therefore, the phenomenon described here provides a new insight regarding mechanical transmission of messages for tissue homeostasis and beyond.

II. EXPERIMENTAL OBSERVATION OF LONG-RANGE FORCE PROPAGATION

We cultured an epithelial monolayer on a gel plated on a glass base [Fig. 1(A)]. The gel has a weak adhesion to the glass base and this loose attachment at the gel-glass interface allows the gel to slip on the glass and hence the deformation of the gel substrate depends on time. We applied a UV laser at the center of the monolayer to damage the DNA of a single cell and to induce apoptosis. A few minutes after ablation, a concentric wave of gel deformation was observed [Fig. 1(B) top and middle].

The deformation dynamics of the gel was captured by the fluorescent beads embedded at the surface, a technique commonly called traction force microscopy (TFM). We tracked fluorescent beads on the images and measured a radial

displacement for each bead, the origin being defined by the apoptotic cell. By averaging the radial displacement over the beads located in the distance $\sim r$ from the center, we obtained the scalar displacement field $u_r(r)$ (red curves in the bottom panel of Fig. 1(B); See Materials and Methods for beads tracking and measurement).

The concentric wave was characterized by a strong peak in the beads displacement field $u_r(r)$ moving outward from the cell extrusion point. The wave moved slowly over a distance of 2 cell diameters in the first 10 minutes [Fig. 1(B) bottom] This happened even with a very thick substrate, *e.g.* with $\sim 50 \mu\text{m}$ thickness, which is larger than a typical cell diameter. The peak separates the space into two regions with inward and outward movement of beads [Fig. 1(C)] and nearly 40 mins after ablation, the beads displacement field starts to stabilize.

The remarkable feature of beads displacement $u_r(r)$ is the emergence of a strong peak. Fig. 2(A, insets) shows the time evolution of the position of peak r_{peak} and the peak value u_{peak} for various samples. The propagation slows down with time t and the evolution of peak position r_{peak} can be well fitted by a function of the following form

$$r_{peak}(t) = r_{peak}^\infty \left(1 - e^{-\sqrt{(t-t_0)/\tau}}\right), \quad (1)$$

where r_{peak}^∞ is the furthest position the peak can reach, t_0 is the onset time of the deformation and τ is the timescale for the peak to stop propagation. These three parameters are found through fitting the data for each sample.

The peak positions $r_{peak}(t)$ of all samples then collapse to a rescaled peak position \tilde{r}_{peak} with these fitting parameters [Fig. 2(A), top]:

$$\tilde{r}_{peak}(t) = \frac{r_{peak} \left(\frac{t-t_0}{\tau}\right)}{r_{peak}^\infty} \sim 1 - e^{-\sqrt{(t-t_0)/\tau}}. \quad (2)$$

Similarly, the corresponding peak height u_{peak} can be rescaled using t_0 and τ fitted from r_{peak} as

$$\tilde{u}_{peak}(r, t) = \frac{u_{peak} \left(\frac{t-t_0}{\tau}\right)}{u_{peak}^\infty} \quad (3)$$

where u_{peak}^∞ is the fitted maximal value for u_{peak} . As shown in the bottom panel of Fig. 2(A), the rescaled peak heights \tilde{u}_{peak} collapse to a nonmonotonic trend: for time $t - t_0 \ll \tau$, \tilde{u}_{peak} grows in a diffusive way (dashed line), *i.e.*, $\propto \sqrt{t}$; yet, for time $t - t_0 \gg \tau$, the \tilde{u}_{peak} slowly decreases. Therefore, the time τ separates the whole process into two stages in time.

During the growth (stage I, $t - t_0 < \tau$), there exists a negative correlation between the magnitude of peak and the propagation speed characterized by $v_{peak}(t) = \Delta r_{peak}(t)/\Delta t$ (Δ denotes the difference between two consecutive time points). As shown in Fig. 2(B), $v_{peak}(t)$ calculated over all the samples in stage I ($t - t_0 < \tau$) is plotted against the magnitude of peak $u_{peak}(t)$, and the black straight line corresponds to $v_{peak}(t)u_{peak}(t) = 0.4 \mu\text{m}^2/\text{min}$. This infers that a faster propagation of the deformation corresponds to a smaller extent of the deformation.

Another feature of the displacement field worth noticing is the slopes of the rise and decay around the peak. In Fig. 2(C), we exhibit a typical sample with its smoothed displacement over 11 minutes after apoptosis in a log-log plot. The near-center displacement $u_r(r < r_{peak})$ grows essentially in a linear way with respect to r , whereas the slope of decay in the displacement field $u_r(r > r_{peak})$ follows essentially a $1/r$ dependency. To investigate the tails exponent of u_r quantitatively, we plot the rescaled displacement $\tilde{u}_r = u_r/u_{peak}$ for multiple samples in Fig. 2(D). Experimental noises from optical defects (which we estimated to be on the order of $0.03 \mu\text{m}$) have been removed from the data and thus improving the quality of the fit. The inset of Fig. 2(D) shows the sample-wise fitted tail powers which has a mean -1.00 ± 0.18 (90% confidence interval, two gray lines).

III. THEORETICAL MODEL AND RESULTS

Next, we addressed the physical mechanism generating this long-range concentric propagation of gel deformation field. By referring to the experimental results, we construct a theory focusing on the gel mechanics with a surface stress field exerted by the tissue. This choice corresponds to our assumption that the tissue processes are decoupled from the gel mechanics.

3D elastic gel model

The creeping time of the PDMS gel used in our experiments is roughly 2 seconds, which is far shorter than the timescale of our interest. Therefore, we just model the gel as a pure elastic material. Considering the axisymmetry in

our problem, the model is set in cylindrical coordinates [See Fig. 1(D)]. Since the beads in experiments were observed in terms of radial displacements, here, we only explain the radial deformation part in the model. Comprehensive explanations of our theory is provided in Materials and Methods.

We construct the theory relying on only linear elasticity of an incompressible gel. The radial displacement field $u_r(r, z, t)$ is a function of radial distance from the center r , the vertical position $z < h$, and the time t , where h is the height of the gel. According to the force balances inside the gel and the incompressibility condition, the spatial profile of u_r obeys

$$\frac{\partial^2 u_r}{\partial r^2} + \frac{1}{r} \frac{\partial u_r}{\partial r} - \frac{u_r}{r^2} + \frac{\partial^2 u_r}{\partial z^2} - \frac{2}{\hat{G}} \frac{\partial P}{\partial r} = 0, \quad (4)$$

where P is the pressure field, which is given through the incompressibility condition, and \hat{G} is an effective shear modulus of the gel.

The only external forces are the shearing forces on the surface $z = h$ and at the bottom $z = 0$:

$$\begin{cases} \sigma_{rz}|_{z=h} = S(r, t) \\ \sigma_{rz}|_{z=0} = \xi \frac{\partial u_r}{\partial t} \Big|_{z=0} \end{cases}, \quad (5)$$

where σ_{rz} is the shear stress defined as

$$\sigma_{rz} = \frac{\hat{G}}{2} \left(\frac{\partial u_r}{\partial z} + \frac{\partial u_z}{\partial r} \right) \quad (6)$$

with the vertical displacement $u_z(r, z, t)$. On the gel surface, $S(r, t)$ is an unknown form of stress field exerted by the cells and we name this term $S(r, t)$ “surface stress” in what follows. At the bottom of the gel, ξ is the friction coefficient that describes the force-velocity relationship during the gel sliding on the glass. For the $z = h$ condition, we have assumed that the change of height over time and space is negligible compared to the magnitude of h itself and thus ignored the tilt of the surface. We also fix h to be a constant.

With specific boundary conditions in our problem (see Materials and Methods), the structure of Eq. 4 allows for the derivation of a general solution by transforming the equation into the wavenumber domain through Hankel transform of order 1. The solution can be represented as a space(2D)-time convolution between the surface stress term and a memory kernel:

$$u_r(r, z, t) = \frac{1}{2\pi} S(r, t) \ast \ast \ast M(r, z, t), \quad (7)$$

where the operator “ $\ast \ast \ast$ ” represents the convolution of two functions over 2D space and time:

$$f_1 \ast \ast \ast f_2(r, t) = \int_{-\infty}^{\infty} dt' \int_{-\infty}^{\infty} dr' \int_0^{2\pi} d\phi r' f_1(\vec{r}', t') f_2(\vec{r} - \vec{r}', t - t').$$

For $r > 0$, this is equivalent to

$$f_1 \ast \ast \ast f_2(r, t) = 2\pi \int_{-\infty}^{\infty} dt' \int_0^{\infty} dk k J_1(kr) F_{1,n}(k, t') F_{2,n}(k, t - t'), \quad (8)$$

where J_1 is the Bessel function of first kind, and $F_{1,n}$ and $F_{2,n}$ are Hankel transforms of f_1 and f_2 from r -domain to the wave-number k -domain. The order $n = 1$ is chosen for our solutions. We also define the notation “ $\ast \ast$ ” for the 2D convolution over space as

$$f_1 \ast \ast f_2(r) = \int_{-\infty}^{\infty} dr' \int_0^{2\pi} d\phi r' f_1(\vec{r}') f_2(\vec{r} - \vec{r}'), \quad (9)$$

with the same convolution identity applied in Eq. 8. Finally, 1D convolution “ \ast ” is defined as the convolution over time.

The memory kernel M in wavenumber k domain can be decomposed into two time-dependent kernels:

$$\begin{aligned} M(k, z, t) &= M_s(k, z, t) + M_f(k, z, t) \\ &= m_s(k, z) \delta(t) + m_f(k, z) M_0(k, t), \end{aligned} \quad (10)$$

where the first kernel M_s has a time-dependency represented by a Dirac's delta function $\delta(t)$, and the second kernel M_f depends on friction in an exponential decay form:

$$M_0(k, t) = \exp \left[-\frac{k \sinh(kh) \cosh(kh) + kh}{\xi \cosh^2(kh) + (kh)^2} t \right] \Theta(t). \quad (11)$$

The dependency of coefficients m_s and m_f on z and r is shown in Fig. 3(A). The kernel M_s is dominant at the surface ($z = h$) while the friction-dependent kernel M_f plays a stronger role at the bottom ($z = 0$). Meanwhile, M_s overwhelms M_f near the center $r < h$, indicating that friction-dependent dynamics is negligible near the center.

Detailed analysis (See SI) of the kernel $M(r, z, t)$ unveils that if the elapsed time t surpasses a critical timescale $t_c = h\xi/\hat{G}$, the z -dependency in the kernel becomes negligible and M_f obeys a dynamic scaling

$$M_f(r, t) \propto \tilde{M}_f \left(r / \sqrt{2\hat{G}ht/\xi} \right), \quad (12)$$

which accounts for the propagation dynamics in the substrate irrespective of the dynamics in the external source term $S(r, t)$. In contrast, if the elapsed time is significantly shorter than the critical timescale t_c , i.e., $t \ll h\xi/\hat{G}$, the friction-dependent kernel M_f vanishes and the kernel M_s stands out. Therefore, the final solution under the friction-independent kernel M_s is:

$$u_r(r, z, t) = \frac{1}{2\pi} S(r, t) * m_s(r, z). \quad (13)$$

As shown in Fig. 3(A), the coefficient m_s grows with z from zero, and reaches a maximal value at the surface:

$$m_s(k, h) = \frac{\sinh(kh) \cosh(kh) + kh}{\cosh^2(kh) + (kh)^2} \quad (14)$$

which is independent of time. Note that this solution is valid when $t \ll h\xi/\hat{G}$, which means that the friction ξ is large enough compared with gel's elastic forces (non-slippage), or the gel is thick enough, or the elapsed time is short enough. Therefore, this solution applies to a nonslippery setting of gel (rigidly bonded to the glass bases). The independence of time in the memory kernel suggests that there is no transmission of forces at long distances and all the dynamics in the substrate is instantaneous and local as expressed by $S(r, t)$.

Models of surface stress field

The external stress field at the surface $S(r, t)$ is transmitted from the tissue through focal adhesion patches. Choosing a form for this term implies a corresponding hypothesis for tissue biomechanics. Evidence shows that such force is not provided by the crawling of cells [27]. The breakdown of intercellular junctions could be a viable mechanism to release the stress previously stored in those junctions on a very short time-scale and thus push the substances away from the apoptotic cell [28]. This transient process generates a spatial stress distribution which transmits to the gel surface. The same experiment also found that the sliding of focal adhesions is negligible at the interface between the cell layer and the gel, indicating that the force is transmitted through the elastic deformation of integrins and hence the external stress could persist for some time. Yet, it is unknown how the stress is distributed in space and how it evolves with time because of other slow biomechanics. In this section, we investigate the dynamics of a gel under three natural patterns of surface stress field, $S(r, t)$, and see if the experimental observations can be recapitulated.

Diffusive propagation given by a simple surface stress profile

For the sake of simplicity, we first choose a power-law dependence for the decay of $S(r, t)$ over the distance r from the center:

$$S(r, t) = s \left(\frac{\varepsilon}{r} \right)^q \Theta(r - r_0) \Theta(t - t_0), \quad (15)$$

where s is the coefficient for the magnitude of prestress in tissue, r_0 is the onset position of this stress, t_0 is the time for the release of stress, and ε is the cell radius, which also determines the scale of spreading distance of the force. The function Θ is a Heaviside step function. Since the roles of t_0 is trivial in the calculation, we set $t_0 = 0$ in the

following demonstration. The role of r_0 is case-dependent, and we present the explanations in SI. Here we assume the simplest case where $r_0 = 0$ (refer to SI for the discussion on the cases with $r_0 > 0$). The reason why we use power law decay instead of others such as exponential ones is to avoid additional length scale at this moment. The power q is chosen to be $0 < q < 3$ to guarantee the convergence of the Hankel transform with $S(r, t)$.

The displacement field with Eq.15, following the solution of the above 3D elastic gel theory, is given by

$$u_r(r, z, t) = \frac{1}{2\pi} s \left(\frac{\varepsilon}{r} \right)^q \Theta(r) * * (\Theta(t) * M(r, z, t)). \quad (16)$$

Figure 3(B) shows the numerical results of displacement fields near the surface $u_r(r, z = 0.9h, t)$ (red) for the case of $q = 1$ with dimensionless time $\tilde{t} = t/t_c = t\hat{G}/h\xi$. For comparison, the solution under nonslippery conditions $u_r^n(r, z = 0.9h, t = 0)$ and under 2D approximation $u_{r,2D}(r, t)$ are also shown in blue dashed curves and black curves (See Materials and Methods for the calculation of these two solutions).

For $t < t_c$, the displacement field $u_r(z = 0.9h)$ (red curves) has a peak magnitude close to $s\varepsilon/\hat{G}$ in the near field $r < h$, the same as that with a nonslippery condition (blue curves; This magnitude will increase with h , see SI). This displacement is transient, caused by the shear deformation of the gel. When t surpasses t_c , the far field of $u_r(r > h, z = 0.9h)$ transitions dynamically from $u_r^n(r > h)$ to $u_{r,2D}(r > h)$. Notice that all the tails of these solutions decay as $1/r$, which agrees well with the tail power -1 found in experiments [Fig.2(C,D)].

Figure 3(B) bottom shows that the peak positions and heights of $u_r(z = 0.9h)$ (red marks and curve) and $u_{r,2D}$ (black marks and curves) collapse to the same curves which grow diffusively with time when $t \gg t_c$ and a propagating peak emerges from $r \sim h$. These results suggest that a 2D approximation theory is sufficient to explain the peak-propagation dynamics at the late time regime.

Therefore, for the sake of simplicity and for our purpose of studying the peak propagation phenomena, we would hereafter focus on the dynamics of $u_{r,2D}$ which allows analytic calculations. The analytical form of $u_{r,2D}$ is the convolution of the source $S(r)$ with the memory kernel M_{2D} , corresponding to the 2D limit (See Materials and Methods):

$$\begin{aligned} u_{r,2D}(r, t) &= \frac{1}{2\pi} S(r) * * M_{2D}(r, t) \\ &\sim \frac{s\varepsilon^q}{2\hat{G}h} r^{2-q} \Theta \left(\sqrt{\frac{2\hat{G}ht}{\xi}} - r \right) + \frac{s\varepsilon^q t}{2\xi r^q} \Theta \left(r - \sqrt{\frac{2\hat{G}ht}{\xi}} \right). \end{aligned} \quad (17)$$

A propagation of the peak is found with $0 < q < 2$. Particularly, \bar{u}_r grows with r^{2-q} for $r < r_{peak}$ and decays with $1/r^q$ for $r > r_{peak}$ in space and a crossover from the growth to decay occurs near $r \sim r_{peak}$. As seen in Eq.17, the power of the decaying tail depends on the choice of q . Among them, for $q = 1$, the tail power is -1 , which indeed matches the result shown in Fig. 3(B) top. Therefore, through the comparison with the experimental observation [Fig. 2(D)], we fix q to be 1 in the following.

The peak of displacement $u_r(r)$ locates at

$$r_{peak}(t) = \sqrt{\frac{2\hat{G}ht}{\xi}}, \quad (18)$$

and if $q = 1$, the magnitude of peak is

$$u_{peak}(t) = Z s \varepsilon \sqrt{\frac{t}{2\hat{G}h\xi}}, \quad (19)$$

where

$$Z = \int_0^\infty dx J_1(x) \frac{1 - e^{-x^2}}{x^2} \sim 0.48227. \quad (20)$$

Both the dynamics of peak position and magnitude grow with \sqrt{t} . (Detailed calculations are presented in SI.) Accordingly, the speed of peak propagation is

$$v_{peak} = \sqrt{\frac{\hat{G}h}{2t\xi}}, \quad (21)$$

which is enhanced by a slipperiness of gel base (smaller ξ) or a large bulk stiffness of gel (larger $\hat{G}h$) and meanwhile, the speed of peak propagation slowdowns with time.

Moreover, the speed is inversely proportional to u_{peak} independently of time as

$$v_{peak} = \frac{Zs\varepsilon}{2\xi} u_{peak}^{-1}. \quad (22)$$

This reciprocal relationship between speed and magnitude of the peak implies that a faster propagation corresponds to a smaller peak, which agrees with the experimental facts well [Fig. 2(B)].

Longtime non-diffusive propagation

In our experiments, we also observed the slowdown of propagation and decay in the peak magnitude for durations longer than several tens of minutes. This deviation at the later stage from the simple surface stress results could also be explained by our theory if the spatial distribution and dynamics of the surface stress field $S(r, t)$ is modeled in more complete ways partly taking into account biomechanical activities as follows.

For instance, we consider that there exist a cut off length l in radial space beyond which the gel surface does not feel the impact from cells anymore. This is possible when the intercellular cues far from the apoptotic center are weak as compared with their intrinsic activities. In this case, the surface stress is given by:

$$S(r, t) = s \left(\frac{\varepsilon}{r} \right)^q e^{-r/l} \Theta(t), \quad (23)$$

then the propagation stops around $r_{peak}^\infty \sim 1.5l$ [Fig. 3(C); for $q = 1$].

The intensity of surface stress may decrease with time due to multiple reasons such as the viscoelastic relaxations of tensions in cytoskeletons as well as in connective integrins and the formation of contractile actin-myosin rings around the extruding cell. Figure 3(D) shows the solution with a linear decaying stress:

$$S(r, t) = s \left(\frac{\varepsilon}{r} \right)^q \Theta(t)(1 - ct), \quad (24)$$

where $c \ll 1/t_c$ quantifies a slow decay with time for $q = 1$. The displacement u_r near the center turns to decrease over longer time [Fig. 3(D) top], indicating that the gel near the center is gradually moving inward to the center and meanwhile the magnitude of peak u_{peak} exhibits a nonmonotonic trend of evolution [Fig. 3(D) bottom]. These results can qualitatively explain the emergence of a negative velocity region in the experiment [Fig. 1(C)] and the nonmonotonicity of the u_{peak} dynamics [Fig. 2(A) bottom].

Besides the linear decaying model, other forms may quantitatively reproduce the dynamics observed in experiments. To determine a plausible time-dependency of the surface stress field requires the elucidation of the tissue mechanics coupled with other biochemical processes triggered after apoptosis, which will be a topic for future research.

Detailed derivations of the solutions with these two forms of surface stress are presented in Materials and Methods.

Quantitative validation

Here, we investigate whether our theory with the simple surface stress profile (Eq. 15) can quantitatively explain the experimental observations for the early time regime, based on the following experimental measurable parameters

$$\varepsilon = 10 \text{ } \mu\text{m}, \hat{G} = 10 \text{ } \text{kPa}, h = 50 \text{ } \mu\text{m}. \quad (25)$$

The first crucial test for the validity of our model is to predict the case where the friction is too large for the gel to slide. In our theory, such a strongly-adhesive (nonslippery) base of a gel is modeled by taking a limit of $\xi \rightarrow \infty$ and the corresponding solution is none other than the friction-independent solution given by Eq.13. Under a simple surface stress field (Eq.15, $q = 1$), the displacement field under nonslippery condition is a steady distribution and with its peak magnitude maximized at the surface:

$$u_r^n(r, z = h) \sim \frac{s\varepsilon}{\hat{G}} \quad (26)$$

(refer to SI for detailed calculations), which is constrained solely by the ratio between cell's contractility s and gel's elasticity \hat{G} .

Previous literature shows that the magnitude of tissue prestress s ranges from $10^2 \sim 10^4$ Pa [15, 29]. Given the aforementioned parameter values (Eq.25), the magnitude of u_r^n should range as:

$$0.1\mu\text{m} < u_r^n < 10\mu\text{m}. \quad (27)$$

Experimentally, the measured magnitude of beads displacement is also constrained by the available microscope resolution. If $u_r^n(r)$ is below the resolution threshold, the information about the motions of some beads would be entangled with optical noises that would undermine the quality of the measurement. Figure 4(A) shows typical snapshots of beads displacement with a strongly adhesive (nonslippery) gel in experiments, where the magnitude of averaged beads displacement (red) is far smaller than the resolution ($0.206\ \mu\text{m}/\text{px}$) with a large standard deviation. This indicates that the upper bound of the magnitude of u_r^n should be $\sim 0.1\mu\text{m}$. Combining Eq. 27, we conjecture $u_r^n \sim 0.1\mu\text{m}$ with the tissue prestress $s \sim 10^2$ Pa in our experiments.

Next, we test the validity our model in the weakly adhesive case. Based on Eqs. 26 and 19, the magnitude of the ratio between the peak value with a weakly adhesive gel $u_{peak}(t)$ and the value with a rigid gel u_r^n is approximately

$$\frac{u_{peak}(t)}{u_r^n} \sim \frac{1}{2} \sqrt{\frac{\hat{G}t}{h\xi}}, \quad (28)$$

which is about 10, as shown in Fig. 4(B). By applying Eq. 28, we could also estimate the unknown friction coefficient between gel and glass ξ for the weakly-adhesive case as

$$\xi \sim 2 \times 10^{10} \text{ Pa} \cdot \text{s/m}, \quad (29)$$

which agrees with the magnitudes estimated in previous literature [30]. Then, from Eq. 22 with the parameter values given in Eqs. 25 and 29, the multiplication of the propagation speed v_{peak} and the magnitude of peak u_{peak} is a constant independent of time estimated as

$$v_{peak}u_{peak} \sim \frac{s\varepsilon}{4\xi} \sim 10^{-14} \text{ m}^2/\text{s}, \quad (30)$$

which agrees with the magnitude $10^{-14}\text{m}^2/\text{s}$ found with stage I in experiments [Fig.2(B)]. Furthermore, the critical timescale t_c for the onset of propagation is

$$t_c \sim \frac{\xi h}{\hat{G}} = 50 \text{ s} \sim 1 \text{ min}, \quad (31)$$

which means this onset of propagation would not be clearly observed in our experiment with time resolutions on a minute-scale. All these quantitative agreements with the experiments confirm the validity of our model.

Physics underlying the propagation in substrate

So far, we have reproduced the wave dynamics with a strong peak using our theoretical model and demonstrated its quantitative validity. For a more intuitive understanding of the mechanism, we next analyze our theory in more details and demonstrate the mechanism behind this phenomenon.

First of all, we should notice that the full details of the elastic gel is not necessary to explain the emergence of the propagation phenomenon. To highlight the essence of the mechanism, we calculated the simplified model in which pressure inhomogeneity is neglected. (See “Simplified theory and the solution” in SI.) We found that even such simplified theory qualitatively reproduces the above-mentioned results, suggesting that, for this peak propagation, the pressure inhomogeneity is not essential. The propagation of u_r itself is sufficient to cause this single-peak wave propagation.

We thus look into the radial displacement $u_r(r)$ at each position r with a weakly-adhesive base under a persisting surface stress field $S(r)$ [Fig. 4(C) top]. We find that $u_r(r)$ at a given r has a sigmoid-like growth as it starts from an initial non-zero value and gradually saturates at another value over time. Since in our theory the substrate gel itself is elastic and the time-dependence can only arise through the friction at the bottom, the initial and final regimes should correspond to the shear deformation with a fixed bottom boundary and the bulk stretch for which the gel’s bottom slips and is completely relaxed, respectively. The stretching happens earliest at center and with a small friction, stretching mode expands fast, whereas with a large friction, the gel stays longer under sheared deformation.

We next discuss what determines the r -dependence in the magnitude of displacement u_r in shear and stretch-regimes. (Compare blue and orange curves in Fig. 4(C) top.) For this purpose, we perform a simple analysis on the

general solution (Eq.7) to highlight its r -dependence by taking the average over z . Assuming $S(r, t) = S(r)\Theta(t)$, we can derive the displacement field averaged over z under pure shearing and pure stretching as:

$$\begin{aligned}\bar{u}_{\text{shear}}(r) &= \frac{1}{h} \int_0^h u_r(r, z, \xi \rightarrow \infty) dz \\ &= \frac{S(r)}{2\pi\hat{G}} * * \mathcal{H}_1^{-1} \left\{ \frac{h}{\cosh(kh)^2 + (kh)^2} \right\} \\ &\propto S(r),\end{aligned}\quad (32)$$

and

$$\begin{aligned}\bar{u}_{\text{stretch}}(r) &= \frac{1}{h} \int_0^h \bar{u}_r(r, z, \xi \rightarrow 0) dz \\ &= \frac{S(r)}{2\pi\hat{G}} * * \mathcal{H}_1^{-1} \left\{ \frac{1/k}{(\sinh(kh)\cosh(kh) + kh)} \right\} \\ &\propto \int_0^r S(r') r' dr',\end{aligned}\quad (33)$$

respectively. The notation \mathcal{H}_n^{-1} means the inverse Hankel transform of order n . Clearly, u_{stretch} is the accumulated local deformations from the center ($r = 0$), which has a distinct radial dependency from that of u_{shear} . The negative r -dependence of u_r in the shear regime (small t region in Fig. 4(C)) is due to our assumption that the surface stress decaying over space, $S(r) \sim 1/r^q$. The positive r -dependence of u_r in the stretch regime (large t region in Fig. 4(C)) is due to the accumulation of deformations from the center, $r = 0$.

To finalize the study of the mechanism, we comment on the following two facts. Firstly, where $r \ll \sqrt{2\hat{G}/(\xi h)} \times t^{1/2}$, the kernel yielding u_{stretch} becomes dominant (See Eq. 62 in Materials and Methods). This suggests that the regime of u_{stretch} expands out from $r = 0$ like normal diffusion. Secondly, as long as we assume a decaying form of Eq. 15 with $0 < q < 2$, the emergent u_{stretch} has an opposite trend in r -dependence against u_{shear} , which leads to a strong peak at the transition boundary from the stretching to shearing regimes in space [Fig. 4(D)].

It is to be noted that, if we regard $u_r(r, h)/h$ in Fig. 4(C) as an effective shear strain in the gel, then its time-evolution at any local position r behaves like the creeping of a type of viscoelastic substrate with a rigidly bound base and the creeping time is proportional to $r^2\xi/\hat{G}h$ [Fig. 4(C) bottom, where the creeping curve of a kind of viscoelastic motif named Zener model is shown]. Although our system is an elastic material with a weakly adhesive base and exhibits a specific inhomogeneity and anisotropy of viscoelasticity where elasticity is absent along vertical direction and viscosity is absent along the radial direction, it exhibits a mechanical features similar to the viscoelastic gel.

IV. SUMMARY AND DISCUSSION

Summary

In this article, we reported a novel form of long-range force propagation in tissues without the presence of dynamic cellular events such as cell division and migration. This propagation of force was first experimentally observed in substrates that weakly adhered to underlying base, over a period of several hours after the ablation of a single cell [Figs. 1(A)-(C), and Fig. 2]. We studied the mechanism using a model based on linear elasticity theory [Figs. 1(D) and Fig. 3], and found with theoretical analyses that the force propagation in substrate originates from the expansion of stretching mode in the substrate due to the relative sliding between substrate layers under a static stress field exerted by the tissues (Fig. 4).

This substrate deformation is peculiarly characterized by a pronounced peak, whose propagation speed is enhanced by a looser attachment between substrate layers or by a stiffer substrate. We confirmed that the friction coefficient ξ at the gel-glass interface evaluated by our theory (Eq. 29) agrees in magnitudes with the plausible values found in the literature. Our experiment also suggested that the propagation speed v_{peak} is inversely proportional to the magnitude of peak u_{peak} with a robust constant, $v_{\text{peak}}u_{\text{peak}} \sim 10^{-14}\text{m}^2/\text{s}$, in the stage where diffusive propagation manifests (< 15 min) in experiments [Fig. 2(C)]. This reciprocal relationship between propagation speed and deformation magnitude is self-consistently captured by our theory in the quantitative level (Eq.30).

Scales of the observed wave

apoptosis triggers a series of biochemical and biomechanical events across multiple time scales for the sake of tissue homeostasis. Calcium waves appear within tens of seconds around the apoptotic cell, followed by the polarization of surrounding cells after ten minutes [25, 31], and probably by division of the cells near the apoptotic range several hours later. The new type of elastic propagation which we found here emerges in between these two time scales.

The speed of propagation is around $0.1\mu\text{m/s}$, which is comparable to the slowest instances of mechanical oscillations in tissues, where the force propagation is realized through viscoelastic properties of tissues [32–34]. The force propagation found in our case is novel in the sense that it propagates in elastic substrates even with a non-dynamic stress field in tissue and the wave in our case is propagating with a single peak rather than traveling waves.

Regarding the spatial scale of the wave, the peaks of gel displacement propagate over a distance of 2-3 cell diameters from the center in experiments. Our theory suggests that the propagation distance is constrained by a cutoff range around the apoptotic cell. Mechanical responses can have long-range correlations in tissues [35–37] and the correlation length scale is determined by the competition between strength of intercellular mechanics and other effects that decorrelate the forces among cells. Therefore, the cutoff range in our theory is the effective area in which the intercellular force transmissions overpowers the decorrelating factors such as the intrinsic cell activities and thermal noises from subcellular and extracellular environment. This range can be associated with stiffness, fluidity (cell-cell rearrangement) and cell cycle activities of a tissue.

An assumption on time evolution of tissue stress

During propagation, the peak can separate the space into regions undergoing inward and outward movement in substrate. Our model results demonstrate that this behavior will appear if the stress exerted by the tissue slowly decays with time. Theory demonstrates that this slow decay also brings the onset of stage II where the peak magnitude decays with time. One possible mechanism for this slow decay is the natural relaxation of forces among cells or between cell and substrate as the substrate deforms [38]. Tissue viscoelasticity may also play a role to induce temporal changes in the spatial stress distributions. Another possible mechanism could be the appearance of forces globally pulling the cells back into the center. The timescale for E-cadherins to accumulate around the extruding cell is roughly 20 minutes after the ablation [25, 31], comparable to the onset time of stage II in experiments and therefore, the formation of contractile actin-myosin ring around the extruding cell could be another viable mechanism for the slow decay.

Cell-substrate mechanical regulations

Recently, it was reported that substrate strain regulates cell mechanosensing [39]. It is to be noted that dynamics of substrate deformation, which we analyzed in this article, also manifests as a propagation of strain field in both radial and angular direction as:

$$\text{radial strain : } \epsilon_{rr} = \frac{\partial u_r}{\partial r}, \text{ angular strain : } \epsilon_{\varphi\varphi} = \frac{u_r}{r}. \quad (34)$$

Near the center ($r < r_{peak}$), cells can sense a local stretching strain in the substrate whereas far from center ($r > r_{peak}$), cells sense the elongation of substrate merely along the angular direction and contraction of substrate along the radial direction. Since cells are sensitive to local strain in the substrate (especially to the stretching strain) for regulating their behaviors [39], mechanosensing activities such as YAP nuclear translocation [40, 41] are expected within this expanding stretched substrate region. The cellular responses to ECM deformation can cause temporal modifications in cellular mechanics and actively influence some major contributors to the deformation propagation such as the cutoff range and the spatial stress distribution in tissues. The effect of such active responses needs more investigations from both theoretical and experimental viewpoint.

Finally we should stress the importance of dynamic remodeling of substrate structure. A weakly adhesive substrate that facilitates inter-layer sliding is core for the emergence of this novel form of force propagation *in vitro*. *In vivo*, the tissue substrates are composed of multiple layers of ECM [42] such as basement membrane and lamina propria and other connective tissues. The biopolymer linkages between these layers would not be as rigid as prepared in conventional TFM experiments because of continuous ECM remodeling. If the turnover of attachment and detachment of ECM components is sufficiently frequent at some places, “sliding” should innately occurs there when external stresses are applied. ECM remodeling will depend on both the constituents and the geometry of the system and may exhibit strong inhomogeneity and anisotropy. The theory we have presented here could be extended to construct theories for force propagation through ECM undergoing more generic types of remodeling.

MATERIALS AND METHODS

Experiment

A monolayer of MDCK cells or MKN28 cells was cultured on a PDMS gel (CY52-276A:CY52-276B=1:1, Dow Corning) overlaid on a glass-bottom Petri dishes (IWAKI). The thickness of the gel is 50 μm , and its Young's Modulus is 15kPa with a Poisson ratio 0.499. Fluorescent (red or far-red, Invitrogen) beads are embedded at the surface of the gel to capture the displacement of the gel surface. A strongly adhesive (non-slipping) base of a gel was prepared by silanizing a glass-bottom Petri dishes with 3-aminopropyl trimethoxysilane (APTES, Sigma). A weakly adhesive (slipping) base of a gel was prepared without APTES. Cells and beads were imaged with a NikonA1R MP laser scanning confocal microscope with Nikon Apo 60x/1.40 oil-immersion objective. Apoptosis was induced using a UV laser as described before [43]. The summary of the experimental setting is summarized in Table 1. Full details of the experimental protocol can be found in Ref. [27].

Calculation of radial displacement

We first preprocessed the images of fluorescent beads for a proper contrast and uniform intensity in grayscale to suppress the impact from optical defects as much as possible. Then, we track each spot in the images by a Python package `trackpy`, and calculate the vector field of displacement from time=0, as shown in Fig.1(B). Then we project all the vectors $\vec{u}(\vec{x})$ at different position $\vec{x} = (x, y)$ onto its radial direction to get the radial displacement $u_r = \vec{u} \cdot \vec{x} / |\vec{x}|$ and turn the vector field to a scalar field $u_r(\vec{x})$. Considering the symmetry about the center (where dwells the apoptotic cell), this 2D scalar field can be further reduced to a 1D field $u_r(r)$ by averaging the beads displacement for beads located at a distance from center r with a range $\Delta r \sim 10\mu\text{m}$. Finally, we perform a Savitzky-Golay filter with subset size $\sim 50\mu\text{m}$ and polynomial order 3 to smooth the averaged displacement.

3D gel model

Let us consider a 3D vector field in a cylindrical system for the gel displacement

$$\hat{u} = u_r \hat{e}_r + u_\varphi \hat{e}_\varphi + u_z \hat{e}_z, \quad (35)$$

where u_r, u_φ, u_z are the scalar field in a 3D cylindrical system. The forces transmitted from the tissue layer is represented by a stress field $s(r, \varphi, z = h)$, and this provides a shearing stress at the surface of the gel and leads to the deformation in the gel characterized by the vector displacement field \hat{u} . Considering the axisymmetry of the exerted stress field, we have:

$$u_\varphi = 0, \quad \partial u_r / \partial \varphi = 0, \quad \partial u_z / \partial \varphi = 0. \quad (36)$$

Based on linear elasticity theory, the strain

$$\epsilon = \frac{1}{2} [\nabla \hat{u} + (\nabla \hat{u})^T] \quad (37)$$

is a second-order symmetric tensor bearing six non-zero components. Considering the symmetry (Eq. 36), the strain tensor in our problem is further simplified to

$$\epsilon = \begin{pmatrix} \epsilon_{rr} & 0 & \epsilon_{rz} \\ 0 & \epsilon_{\varphi\varphi} & 0 \\ \epsilon_{rz} & 0 & \epsilon_{zz} \end{pmatrix} \rightarrow \begin{pmatrix} \epsilon_{rr} \\ \epsilon_{zz} \\ \epsilon_{\varphi\varphi} \\ \epsilon_{rz} \end{pmatrix}, \quad (38)$$

TABLE I. Summary of experiment information.

No.	Base	Cell	Interval	Duration	Sample
1	Slippery	MDCK	1 min	11 min	12
2	Slippery	MKN28	5 min	2 hours	8
3	Nonslippery	MDCK	1 min	11 min	3

where

$$\begin{aligned}\epsilon_{rr} &= \frac{\partial u_r}{\partial r}, \\ \epsilon_{\varphi\varphi} &= \frac{u_r}{r}, \\ \epsilon_{zz} &= \frac{\partial u_z}{\partial z}, \\ \epsilon_{rz} &= \frac{1}{2} \left(\frac{\partial u_r}{\partial z} + \frac{\partial u_z}{\partial r} \right)\end{aligned}\tag{39}$$

are the normal and shear strains with respect to u_r and u_z calculated from Eq. 37.

The stress tensor σ is related to the strain tensor ϵ by a stiffness tensor \hat{E} :

$$\sigma = \hat{E}\epsilon, \tag{40}$$

and in a homogeneous and isotropic material with axisymmetry and Poisson ratio near 0.5 (incompressibility), the stress tensor components simply satisfy

$$\begin{aligned}\sigma_{rr} &= \frac{E}{1+\nu} \epsilon_{rr} - P, \\ \sigma_{\varphi\varphi} &= \frac{E}{1+\nu} \epsilon_{\varphi\varphi} - P \\ \sigma_{zz} &= \frac{E}{1+\nu} \epsilon_{zz} - P, \\ \sigma_{rz} &= \frac{E}{1+\nu} \epsilon_{rz}\end{aligned}\tag{41}$$

with the pressure P being a Lagrange multiplier allowing the deformations to satisfy the incompressibility condition.

The force is balanced in the material as

$$\nabla \cdot \sigma + \hat{F} = \rho \frac{\partial^2 \hat{u}}{\partial t^2}, \tag{42}$$

where σ is the stress tensor and \hat{F} is the body force field and the right-hand term is the inertia. In a micro-scale material, the inertia term is negligible and there is no body force in our problem. Hence, we apply the force balance equation

$$\nabla \cdot \sigma = 0, \tag{43}$$

and again due to the axisymmetry, the force balance along the radial direction is:

$$\frac{1}{r} \frac{\partial}{\partial r} (r \sigma_{rr}) + \frac{\partial \sigma_{rz}}{\partial z} - \frac{\sigma_{\varphi\varphi}}{r} = 0, \tag{44}$$

and the force balance along the z -direction is:

$$\frac{\partial}{\partial r} (r \sigma_{rz}) + \frac{\partial \sigma_{zz}}{\partial z} = 0. \tag{45}$$

In what follows, we assume that ν is asymptotically close to 1/2, i.e., an incompressible gel. In this case, we can apply the incompressible condition

$$\nabla \cdot \hat{u} = \frac{1}{r} \frac{\partial}{\partial r} (r u_r) + \frac{\partial u_z}{\partial z} = \epsilon_{rr} + \epsilon_{\varphi\varphi} + \epsilon_{zz} = 0. \tag{46}$$

to determine the pressure field $P(r, z)$.

In terms of radial displacement field u_r , vertical displacement field u_z and pressure field P , Eqs. 44-46 lead to the following equations :

$$\frac{\partial^2 u_r}{\partial r^2} + \frac{1}{r} \frac{\partial u_r}{\partial r} - \frac{u_r}{r^2} + \frac{\partial^2 u_r}{\partial z^2} - \frac{2}{\hat{G}} \frac{\partial P}{\partial r} = 0 \tag{47}$$

(Eq. 4 of Section “Theoretical model and results”),

$$\frac{\partial^2 u_z}{\partial r^2} + \frac{1}{r} \frac{\partial u_z}{\partial r} + \frac{\partial^2 u_z}{\partial z^2} - \frac{2}{\hat{G}} \frac{\partial P}{\partial z} = 0. \quad (48)$$

and

$$\frac{\partial^2 P}{\partial r^2} + \frac{1}{r} \frac{\partial P}{\partial r} + \frac{\partial^2 P}{\partial z^2} = 0, \quad (49)$$

respectively, where $\hat{G} = \frac{E}{1+\nu} = 2G$ is 2 times the shear modulus G of the gel.

Solution

Here, we provide the solution to Eqs. 47 - 49 with the following boundary conditions: Two shearing forces on the top and bottom surface (see Eqs. 5 in the main text), zero normal forces to the surface $\sigma_{zz}(z = h) = 0$, a flat bottom $u_z(z = 0) = 0$, together with the finiteness of $u_r(r \rightarrow 0)$, $P(r \rightarrow 0)$, $u_r(r \rightarrow \infty)$ and $P(r \rightarrow \infty)$. See also “Full theory and the detailed derivation of the solution” in SI for the details of boundary conditions and the derivation.

By transforming $u_r(r, z, t)$ into $u_r(k, z, t)$ in wavenumber k -domain by Hankel transform of order 1, the solution is eventually obtained as

$$u_r(k, z, t) = S(k, t) * \left(m_s(k, z) \delta(t) + m_f(k, z) M_0(k, t) \right), \quad (50)$$

where $*$ means the 1D convolution (the convolution over time) as given right below Eq. 9. Here,

$$M_0(k, t) = \exp \left[-\frac{k}{\tilde{\xi} R(k, 0)} t \right] \Theta(t) \quad (51)$$

is the time-dependent memory kernel, and the time-independent factors are defined as

$$m_s(k, z) = \frac{1}{\hat{G}} \frac{Q(k, z) R(k, 0) - Q(k, 0) R(k, z)}{k R(k, 0)} \quad (52)$$

which is independent of friction, and

$$m_f(k, z) = \frac{1}{\tilde{\xi}} \frac{Q(k, 0) R(k, z)}{R(k, 0)^2} \quad (53)$$

which depends on friction, with

$$Q(k, z) = \frac{1}{\sinh(kh) \cosh(kh) + kh} \left[\cosh(kh) \cosh(kz) - (kh) \sinh(kh) \cosh(kz) + (kz) \cosh(kh) \sinh(kz) \right] \quad (54)$$

and

$$R(k, z) = \frac{1}{\sinh(kh) \cosh(kh) + kh} \left[\cosh(kh) \cosh(k(h-z)) - (kh) \sinh(kz) - (kz) \cosh(kh) \sinh(k(h-z)) + (kh)(k(h-z)) \cosh(kz) \right]. \quad (55)$$

We can obtain the solution in r -domain by inverse Hankel transform

$$u_r(r, z, t) = \int_0^\infty k dk J_1(kr) u_r(k, z, t). \quad (56)$$

With a persistent surface stress $S(r, t) = S(r) \Theta(t)$, the solution becomes

$$\begin{aligned} u_r(r, z, t) &= \int_0^\infty k dk J_1(kr) S(k) \left(m_s + m_f \frac{\tilde{\xi} R(k, 0)}{k} (1 - M_0) \right) \Theta(t) \\ &= \frac{1}{2\pi} S(r) * * M_p(r, z, t), \end{aligned} \quad (57)$$

where $\mathcal{H}_1\{M_p(r, z, t)\}$ is

$$M_p(k, z, t) = \frac{\Theta(t)}{\hat{G}} \left(\frac{Q(k, z)}{k} - \frac{Q(k, 0)R(k, z)}{kR(k, 0)} \exp \left[-\frac{k}{\tilde{\xi}R(k, 0)} t \right] \right). \quad (58)$$

The notation \mathcal{H}_n means the Hankel transform of order n .

The nonslippery solution ($\xi \rightarrow \infty$) coincides with the transient solution at $t \rightarrow 0$:

$$u_r^n(r, z, t) = \frac{1}{2\pi} S(r) * * M_p^n(r, z), \quad (59)$$

where $\mathcal{H}_1\{M_n(r, z)\}$ is

$$M_p^n(k, z) = M_p(k, z, 0) = m_s(k, z). \quad (60)$$

Therefore, the surface deformation caused by the shear mode when $t \ll t_c$ is

$$u_r^n(r, h) = \int_0^\infty dk \tilde{S}(k, 0) \frac{\sinh(kh)\cosh(kh) + kh}{\cosh^2(kh) + (kh)^2}. \quad (61)$$

On the contrary, when $t \gg t_c$, or equivalently, when under the 2D approximation $h \ll \hat{G}t/\xi$, this memory kernel M_p is simplified to

$$\bar{M}_p(r, t) = M_{2D}(r, t) \equiv \frac{\Theta(t)}{\hat{G}} \mathcal{H}_1^{-1} \left\{ \frac{1 - e^{-2k^2 t/\tilde{\tau}}}{2hk^2} \right\}, \quad (62)$$

where $\tilde{\tau} = \xi/\hat{G}h$. In what follows and in the main text, we will omit $\bar{\cdot}$ in the z -averaged displacement $\bar{u}_r(r, t)$ for the simplicity of notation.

Details of the case with persistent surface stress with a cut-off length

Substituting the form Eq. 23 into Eq. 57 gives the solution as:

$$u_r(r, t) = s\varepsilon \int_0^\infty k dk J_1(kr) \frac{k}{K(K+k)} M_p(k, t), \quad (63)$$

where $K = \sqrt{k^2 + 1/l^2}$. The kernel $k/(K(K+k))$ is exactly the Hankel transform of $e^{-r/l}/r$. By rewriting Eq. 63 into a convolution form we get:

$$u_r(r, t) = \frac{s\varepsilon}{2\pi} \frac{1}{r} * * \mathcal{H}_1^{-1}\{\hat{M}(k, t)\}, \quad (64)$$

where

$$\hat{M}(k, t) = \frac{\Theta(t)}{\hat{G}} \frac{1}{hK(K+k)} M_p(k, t) \quad (65)$$

Since we would like to know long-term behavior of the model, we can use the 2D approximation ($\xi h/\hat{G} \ll t$) so that

$$\hat{M}(k, t) = \hat{M}_{2D}(k, t) \equiv \frac{\Theta(t)}{\hat{G}} \frac{1 - e^{-2k^2 t/\tilde{\tau}}}{2hK(K+k)}, \quad (66)$$

where $\tilde{\tau} = \xi/\hat{G}h$. Clearly, when $t/\tilde{\tau} \ll l^2$, this time-dependent factor could be reduced to M_{2D} (Eq. 62), in which the diffusive scaling is well preserved. By contrast, for long time limit $t/\tilde{\tau} \gg l^2$, the $\hat{M}_{2D}(r, t)$ is reduced to another form that spatially scales with l as:

$$\begin{aligned} \hat{M}_{2D}(r, t \gg l^2 \tilde{\tau}) &= \widetilde{\hat{M}}_{2D}(\tilde{r}) \quad \text{with } \tilde{r} \equiv r/l \\ &= \frac{\Theta(t)}{2\hat{G}} \mathcal{H}_1^{-1} \left\{ \frac{1}{h\sqrt{\tilde{k}^2 + 1}(\sqrt{\tilde{k}^2 + 1} + \tilde{k})} \right\}, \end{aligned} \quad (67)$$

where the inverse Hankel transform \mathcal{H}_1^{-1} is employed from the \tilde{k} - to \tilde{r} -domains.

Details of the case with a decaying surface stress

If the exerted stress slowly decays with time as $S(r, t) = S(r) * (1 - ct)\Theta(t)$, the memory kernel under 2D approximation becomes

$$\begin{aligned} M_d(k, t) &= \frac{\Theta(t)}{2\hat{G}} \int_0^t \frac{e^{-2k^2(t-t')/\tilde{\tau}}}{h\tilde{\tau}} (1 - ct') dt' \\ &= M_{2D}(k, t) - cM_c(k, t) \end{aligned} \quad (68)$$

with

$$M_c(k, t) = \frac{\Theta(t)}{2\hat{G}} \frac{\tilde{\tau}}{h} \frac{2k^2t/\tilde{\tau} + e^{-2k^2t/\tilde{\tau}} - 1}{4k^4},$$

and the final solution $u_r(r, t)$ is

$$u_r(r, t) = \bar{u}_{2D} - \frac{c}{2\pi} S(r) * * \mathcal{H}_1^{-1}\{M_c(k, t)\}. \quad (69)$$

The inverse Hankel transform of $M_c(k, t)$ has the profile similar to that of M_{2D} except that the magnitude of $M_c(k, t)$ grows with time $t^2/\tilde{\tau}$ for $r < \sqrt{2\hat{G}ht/\xi}$. Hence, the final profile of $u_r(r, t)$ has a negative velocity for $r < r_{peak}$.

ACKNOWLEDGMENTS

This research is supported by Mechanobiology Institute (MBI), National University of Singapore. We thank Andrew Wong from MBI science communication core for editing the manuscript and MBI computational core for supporting us about computer-related research activities. We also appreciate Rakesh Das, Alokendra Ghosh and Ayumi Ozawa for valuable discussions.

AUTHOR CONTRIBUTIONS

Y.L., Y.T., J.P. and T.H. designed research. Y.T. designed experiments. T.K and I.Y. conduct the experiments. Y.L., J.P. and T.H. proposed the theoretical model and performed the analytical calculation. Y.L processed the TFM images, performed data analysis, numerical integration, and provided the interpretation of the results. Y.L. and T.H. wrote the manuscript.

[1] Rumi De, Assaf Zemel, and Samuel A. Safran. Dynamics of cell orientation. *Nature Physics*, 3(9):655–659, Sep 2007.

[2] Rumi De and Samuel A. Safran. Dynamical theory of active cellular response to external stress. *Phys. Rev. E*, 78:031923, Sep 2008.

[3] Brenton D. Hoffman, Carsten Grashoff, and Martin A. Schwartz. Dynamic molecular processes mediate cellular mechanotransduction. *Nature*, 475(7356):316–323, Jul 2011.

[4] Yoshiaki Iwadate, Chika Okimura, Katsuya Sato, Yuta Nakashima, Masatsune Tsujioka, and Kazuyuki Minami. Myosin-ii-mediated directional migration of dictyostelium cells in response to cyclic stretching of substratum. *Biophysical Journal*, 104(4):748 – 758, 2013.

[5] Yidan Cui, Feroz M. Hameed, Bo Yang, Kyunghee Lee, Catherine Qiurong Pan, Sungsu Park, and Michael Sheetz. Cyclic stretching of soft substrates induces spreading and growth. *Nature Communications*, 6(1):6333, Feb 2015.

[6] S. A. Gudipaty, J. Lindblom, P. D. Loftus, M. J. Redd, K. Edes, C. F. Davey, V. Krishnegowda, and J. Rosenblatt. Mechanical stretch triggers rapid epithelial cell division through piezo1. *Nature*, 543(7643):118–121, Mar 2017.

[7] Shuichi Asano, Satoru Ito, Mika Morosawa, Kishio Furuya, Keiji Naruse, Masahiro Sokabe, Etsuro Yamaguchi, and Yoshinori Hasegawa. Cyclic stretch enhances reorientation and differentiation of 3-d culture model of human airway smooth muscle. *Biochemistry and Biophysics Reports*, 16:32 – 38, 2018.

[8] Pere Roca-Cusachs, Vito Conte, and Xavier Trepat. Quantifying forces in cell biology. *Nature cell biology*, 19(7):742–751, 2017.

[9] Claire Bertet, Lawrence Sulak, and Thomas Lecuit. Myosin-dependent junction remodelling controls planar cell intercalation and axis elongation. *Nature*, 429(6992):667–671, Jun 2004.

[10] Adam C. Martin, Matthias Kaschube, and Eric F. Wieschaus. Pulsed contractions of an actin–myosin network drive apical constriction. *Nature*, 457(7228):495–499, Jan 2009.

[11] Carl-Philipp Heisenberg and Yohanns Bellaïche. Forces in tissue morphogenesis and patterning. *Cell*, 153(5):948–962, May 2013.

[12] Yusuke Toyama, Xomalin G. Peralta, Adrienne R. Wells, Daniel P. Kiehart, and Glenn S. Edwards. Apoptotic force and tissue dynamics during drosophila embryogenesis. *Science*, 321(5896):1683–1686, 2008.

[13] Xiang Teng and Yusuke Toyama. Apoptotic force: Active mechanical function of cell death during morphogenesis. *Development, Growth & Differentiation*, 53(2):269–276, 2011.

[14] Xavier Trepat, Michael R. Wasserman, Thomas E. Angelini, Emil Millet, David A. Weitz, James P. Butler, and Jeffrey J. Fredberg. Physical forces during collective cell migration. *Nature Physics*, 5(6):426–430, Jun 2009.

[15] Dhananjay T. Tambe, C. Corey Hardin, Thomas E. Angelini, Kavitha Rajendran, Chan Young Park, Xavier Serra-Picamal, Enhua H. Zhou, Muhammad H. Zaman, James P. Butler, David A. Weitz, Jeffrey J. Fredberg, and Xavier Trepat. Collective cell guidance by cooperative intercellular forces. *Nature Materials*, 10(6):469–475, Jun 2011.

[16] Kazuhiro Aoki, Yohei Kondo, Honda Naoki, Toru Hiratsuka, Reina E. Itoh, and Michiyuki Matsuda. Propagating wave of erk activation orients collective cell migration. *Developmental Cell*, 43(3):305 – 317.e5, 2017.

[17] Naoya Hino, Leone Rossetti, Ariadna Marín-Llauradó, Kazuhiro Aoki, Xavier Trepat, Michiyuki Matsuda, and Tsuyoshi Hirashima. Erk-mediated mechanochemical waves direct collective cell polarization. *Developmental Cell*, 53(6):646 – 660.e8, 2020.

[18] Daniel Boocock, Naoya Hino, Natalia Ruzickova, Tsuyoshi Hirashima, and Edouard Hannezo. Theory of mechanochemical patterning and optimal migration in cell monolayers. *Nature Physics*, 17(2):267–274, 2021.

[19] Tatsuya Fukuyama, Hiroyuki Ebata, Yohei Kondo, Kazuhiro Aoki, and Yusuke T. Maeda. Why epithelial cells collectively move against a traveling signal wave. 2020.

[20] Marina Uroz, Sabrina Wistorf, Xavier Serra-Picamal, Vito Conte, Marta Sales-Pardo, Pere Roca-Cusachs, Roger Guimerà, and Xavier Trepat. Regulation of cell cycle progression by cell–cell and cell–matrix forces. *Nature Cell Biology*, 20(6):646–654, Jun 2018.

[21] Rudolf Merkel, Norbert Kirchgeßner, Claudia M. Cesa, and Bernd Hoffmann. Cell force microscopy on elastic layers of finite thickness. *Biophysical Journal*, 93(9):3314 – 3323, 2007.

[22] John M Maloney, Emily B Walton, Christopher M Bruce, and Krystyn J Van Vliet. Influence of finite thickness and stiffness on cellular adhesion-induced deformation of compliant substrata. *Physical Review E*, 78(4):041923, 2008.

[23] Shamik Sen, Adam J. Engler, and Dennis E. Discher. Matrix strains induced by cells: Computing how far cells can feel. *Cellular and Molecular Bioengineering*, 2(1):39–48, Mar 2009.

[24] Amnon Buxboim, Irena L. Ivanovska, and Dennis E. Discher. Matrix elasticity, cytoskeletal forces and physics of the nucleus: how deeply do cells ‘feel’ outside and in? *Journal of Cell Science*, 123(3):297–308, 2010.

[25] Yasuto Takeuchi, Rika Narumi, Ryutaro Akiyama, Elisa Vitiello, Takanobu Shirai, Nobuyuki Tanimura, Keisuke Kuromiya, Susumu Ishikawa, Mihoko Kajita, Masazumi Tada, et al. Calcium wave promotes cell extrusion. *Current Biology*, 30(4):670–681, 2020.

[26] Anh Phuong Le, Jean-François Rupprecht, René-Marc Mège, Yusuke Toyama, Chwee Teck Lim, and Benoît Ladoux. Adhesion-mediated heterogeneous actin organization governs apoptotic cell extrusion. *Nature communications*, 12(1):1–18, 2021.

[27] Takumi Kawaue, Ivan Yow, Anh Phuong Le, Yuting Lou, Mavis Loheras, Murat Shagirov, Jacques Prost, Tetsuya Hiraiwa, Benoit Ladoux, and Yusuke Toyama. Mechanics defines the spatial pattern of compensatory proliferation. *bioRxiv* 10.1101/2021.07.04.451019.

[28] Xiang Teng, Lei Qin, Roland Le Borgne, and Yusuke Toyama. Remodeling of adhesion and modulation of mechanical tensile forces during apoptosis in drosophila epithelium. *Development*, 144(1):95–105, 2017.

[29] Ning Wang, Iva Marija Tolic-Nørrelykke, Jianxin Chen, Srboljub M Mijailovich, James P Butler, Jeffrey J Fredberg, and Dimitrije Stamenovic. Cell prestress. i. stiffness and prestress are closely associated in adherent contractile cells. *American Journal of Physiology-Cell Physiology*, 282(3):C606–C616, 2002.

[30] K Kruse, JF Joanny, F Jülicher, and J Prost. Contractility and retrograde flow in lamellipodium motion. *Physical biology*, 3(2):130, 2006.

[31] Veronica Lubkov and Dafna Bar-Sagi. E-cadherin-mediated cell coupling is required for apoptotic cell extrusion. *Current Biology*, 24(8):868–874, 2014.

[32] Xavier Serra-Picamal, Vito Conte, Romaric Vincent, Ester Anon, Dhananjay T Tambe, Elsa Bazellieres, James P Butler, Jeffrey J Fredberg, and Xavier Trepat. Mechanical waves during tissue expansion. *Nature Physics*, 8(8):628–634, 2012.

[33] M Deforet, V Hakim, HG Yevick, G Duclos, and P Silberzan. Emergence of collective modes and tri-dimensional structures from epithelial confinement. *Nature communications*, 5(1):1–9, 2014.

[34] Carles Blanch-Mercader and Jaume Casademunt. Hydrodynamic instabilities, waves and turbulence in spreading epithelia. *Soft matter*, 13(38):6913–6928, 2017.

[35] Daniel A Fletcher and R Dyche Mullins. Cell mechanics and the cytoskeleton. *Nature*, 463(7280):485–492, 2010.

[36] Ninna S Rossen, Jens M Tarp, Joachim Mathiesen, Mogens H Jensen, and Lene B Oddershede. Long-range ordered vorticity patterns in living tissue induced by cell division. *Nature communications*, 5(1):1–7, 2014.

[37] Guillaume Charras and Alpha S Yap. Tensile forces and mechanotransduction at cell–cell junctions. *Current Biology*, 28(8):R445–R457, 2018.

[38] Nargess Khalilgharibi, Jonathan Fouchard, Nina Asadipour, Ricardo Barrientos, Maria Duda, Alessandra Bonfanti, Amina Yonis, Andrew Harris, Payman Mosaffa, Yasuyuki Fujita, Alexandre Kabla, Yanlan Mao, Buzz Baum, Josè J Mu noz,

Mark Miodownik, and Guillaume Charras. Stress relaxation in epithelial monolayers is controlled by the actomyosin cortex. *Nature Physics*, 15:839–847, 2019.

[39] Valeria Panzetta, Sabato Fusco, and Paolo A Netti. Cell mechanosensing is regulated by substrate strain energy rather than stiffness. *Proceedings of the National Academy of Sciences*, 116(44):22004–22013, 2019.

[40] Sirio Dupont, Leonardo Morsut, Mariaceleste Aragona, Elena Enzo, Stefano Giulitti, Michelangelo Cordenonsi, Francesca Zanconato, Jimmy Le Digabel, Mattia Forcato, Silvio Bicciato, et al. Role of yap/taz in mechanotransduction. *Nature*, 474(7350):179–183, 2011.

[41] Giorgia Nardone, Jorge Oliver-De La Cruz, Jan Vrbsky, Cecilia Martini, Jan Pribyl, Petr Skládal, Martin Pešl, Guido Caluori, Stefania Pagliari, Fabiana Martino, et al. Yap regulates cell mechanics by controlling focal adhesion assembly. *Nature communications*, 8(1):1–13, 2017.

[42] Pengfei Lu, Valerie M Weaver, and Zena Werb. The extracellular matrix: a dynamic niche in cancer progression. *Journal of cell biology*, 196(4):395–406, 2012.

[43] Leyla Kocgozlu, Thuan Beng Saw, Anh Phuong Le, Ivan Yow, Murat Shagirov, Eunice Wong, René-Marc Mège, Chwee Teck Lim, Yusuke Toyama, and Benoit Ladoux. Epithelial cell packing induces distinct modes of cell extrusions. *Current Biology*, 26(21):2942–2950, 2016.

[44] M. C. Marchetti, J. F. Joanny, S. Ramaswamy, T. B. Liverpool, J. Prost, Madan Rao, and R. Aditi Simha. Hydrodynamics of soft active matter. *Rev. Mod. Phys.*, 85:1143–1189, Jul 2013.

[45] Venkat Maruthamuthu, Benedikt Sabass, Ulrich S. Schwarz, and Margaret L. Gardel. Cell-ecm traction force modulates endogenous tension at cell–cell contacts. *Proceedings of the National Academy of Sciences*, 108(12):4708–4713, 2011.

[46] Zhijun Liu, John L. Tan, Daniel M. Cohen, Michael T. Yang, Nathan J. Sniadecki, Sami Alom Ruiz, Celeste M. Nelson, and Christopher S. Chen. Mechanical tugging force regulates the size of cell–cell junctions. *Proceedings of the National Academy of Sciences*, 107(22):9944–9949, 2010.

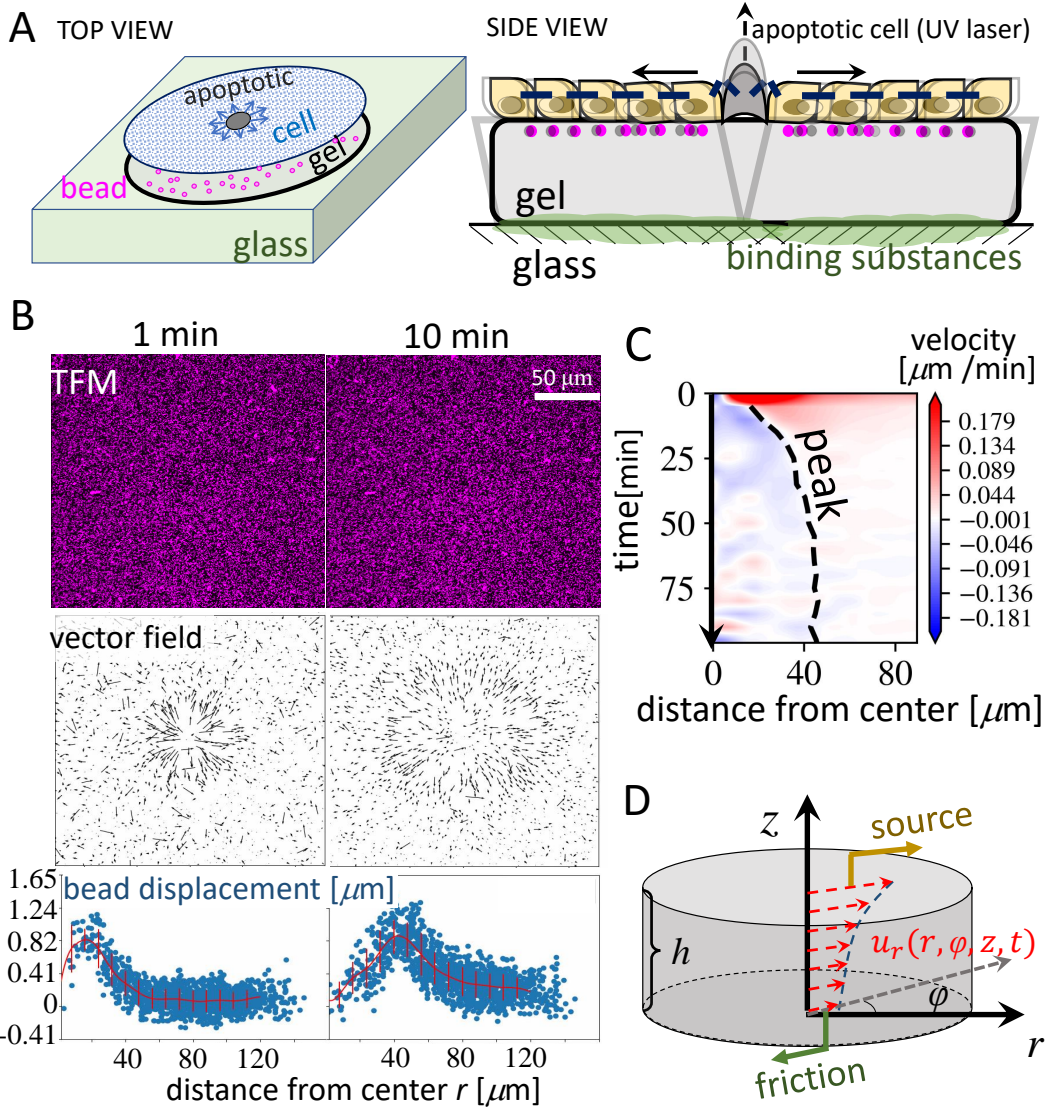


FIG. 1. Experimental setting. (A) Time-dependent traction force microscopy (TFM) for cell apoptosis extrusion. The amount of binding substances is controlled, which is different from a conventional preparation of a gel for traction force microscopy (TFM). (B) Top: images of fluorescent beads under TFM; Middle: vector fields of beads displacement by tracking the beads in the images; Bottom: displacement of beads by projecting the vector field of displacement onto radial direction. Each blue dot corresponds to a single tracked bead and the red curves are the smoothed moving average of the scattered dots. (C) A typical Kymograph for smoothed displacement velocity, which is calculated from the variation of displacement between two consecutive time frames, divided by time interval (5 min). Dashed curve is where the peak of radial displacement locates. (D) 3D elastic material model for the deformation problem in the gel in our experiments

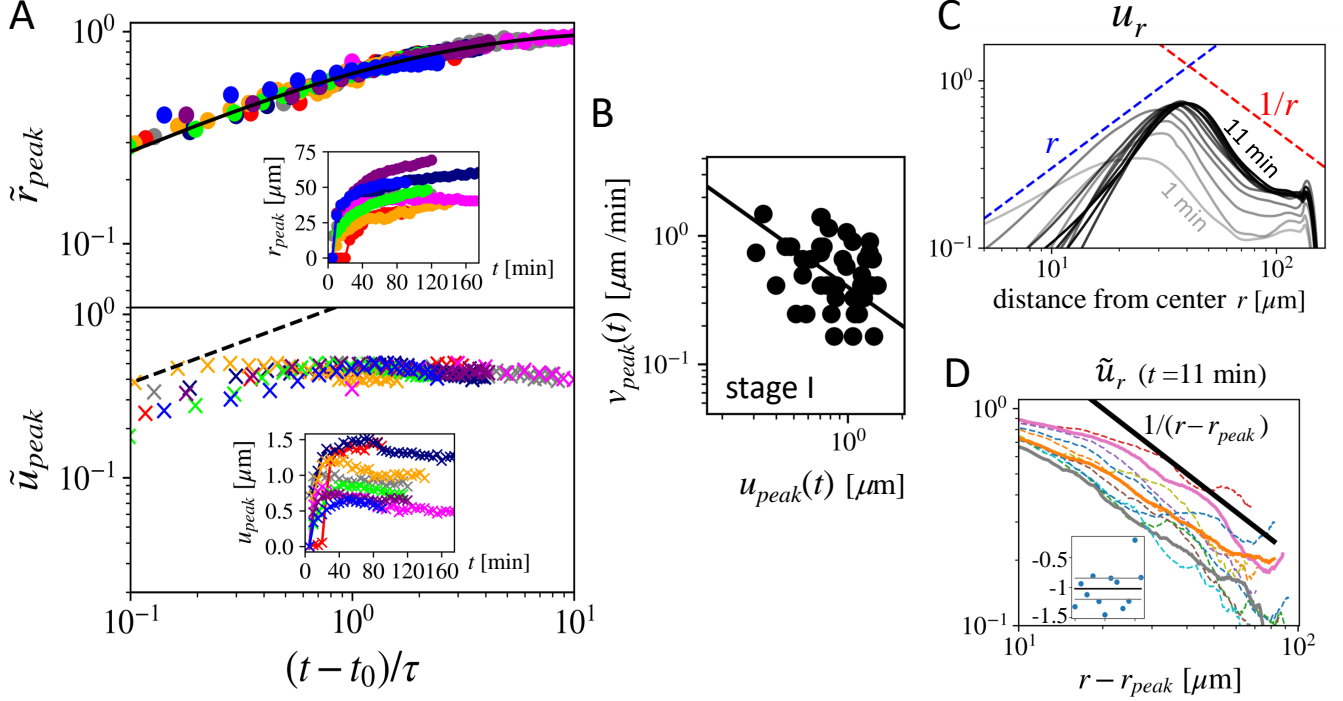


FIG. 2. Substrate dynamics in experiment. (A) The dynamics of the rescaled peak position \tilde{r}_{peak} and rescaled peak magnitude \tilde{u}_{peak} . The black solid curve in the top plot shows the fitting form Eq.1 where a diffusive trend crosses over to a saturating plateau; the black dashed curve in the bottom plot shows a diffusive trend. Two stages in time are separated by the onset of the deviation of \tilde{u}_{peak} from a diffusive behavior. Inset: Original sample-wise peak dynamics. (B) The negative correlation between peak propagation speed v_{peak} and peak magnitude u_{peak} for all the time points within stage I ($t < \tau$). The straight line corresponds to $v_{peak} = 0.4/u_{peak}$. (C) Evolution of smoothed moving average of beads radial displacement u_r over time from 1 min (light gray) to 11 min (black) in a typical sample. (D) Rescaled radial displacement \tilde{u} of multiple samples 11 minutes after apoptosis for the relative distance from peak $r - r_{peak}$. The bold black line corresponds to $\propto 1/(r - r_{peak})$. Inset shows the fitted tail exponents (blue dots) and the bold black line is the average over samples with the two gray lines sketching a 90% confidence interval -1.00 ± 0.18 .

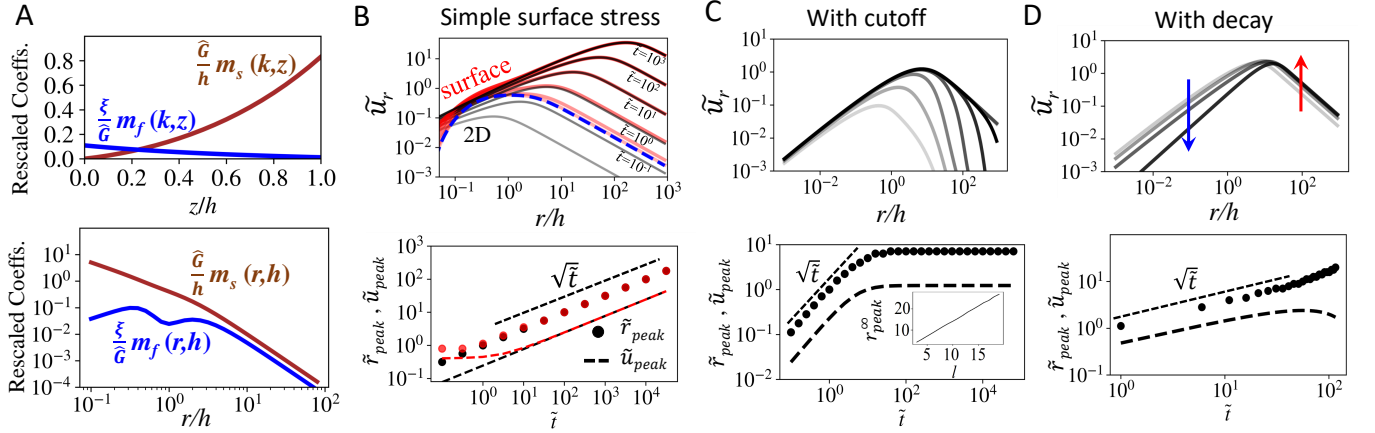


FIG. 3. Theoretical emergence of peak propagation. (A) Top: The z dependency of two coefficients m_s and m_f in the memory kernel for $k = 1/h$. Bottom: the r dependency of m_s and m_f for $z = h$. (B) Solutions with the simple surface stress form given by Eq.15 with $q = 1$. Top: Radial displacement \tilde{u}_r , which is u_r normalized by a coefficient $s\varepsilon/\hat{G}$ at near surface $z=0.9h$ (red) and under 2D approximation (black) for varying dimensionless time $\tilde{t} = t/t_c = t\hat{G}/\xi h$. Bottom: Dynamics of \tilde{r}_{peak} , which is r_{peak} normalized by h (dotted lines) and \tilde{u}_{peak} , which u_{peak} normalized by $s\varepsilon/\hat{G}$ (dashed lines) for the near-surface (red) and 2D approximation model with dimensionless time \tilde{t} . (C) Top: Solution under the surface stress with a cutoff length l (Eq.23) in the model with 2D approximation. Top: Radial displacement u_r normalized by $s\varepsilon/\hat{G}$ for varying time, with $l = 5h$. Bottom: Dynamics of \tilde{r}_{peak} (dots) and \tilde{u}_{peak} (dashed line) with dimensionless time \tilde{t} . Propagation stops at $r_{peak} \sim 1.5l$. Inset: the furthest peak position r_{peak}^∞ is roughly $1.5l$. (D) Solution under the surface stress with a linear decay rate c (Eq.24) in the model with 2D approximation. Top: Radial displacement \tilde{u}_r normalized by $s\varepsilon/\hat{G}$ for varying time for $c = 0.01$. Blue arrow indicates the negative velocity of displacement (inward movement) and the red arrow indicates the positive velocity of displacement (outward movement). Right: Dynamics of \tilde{r}_{peak} (dots) and \tilde{u}_{peak} (dashed line) with dimensionless time \tilde{t} . A nonmonotonic trend in \tilde{u}_{peak} appears for larger time.

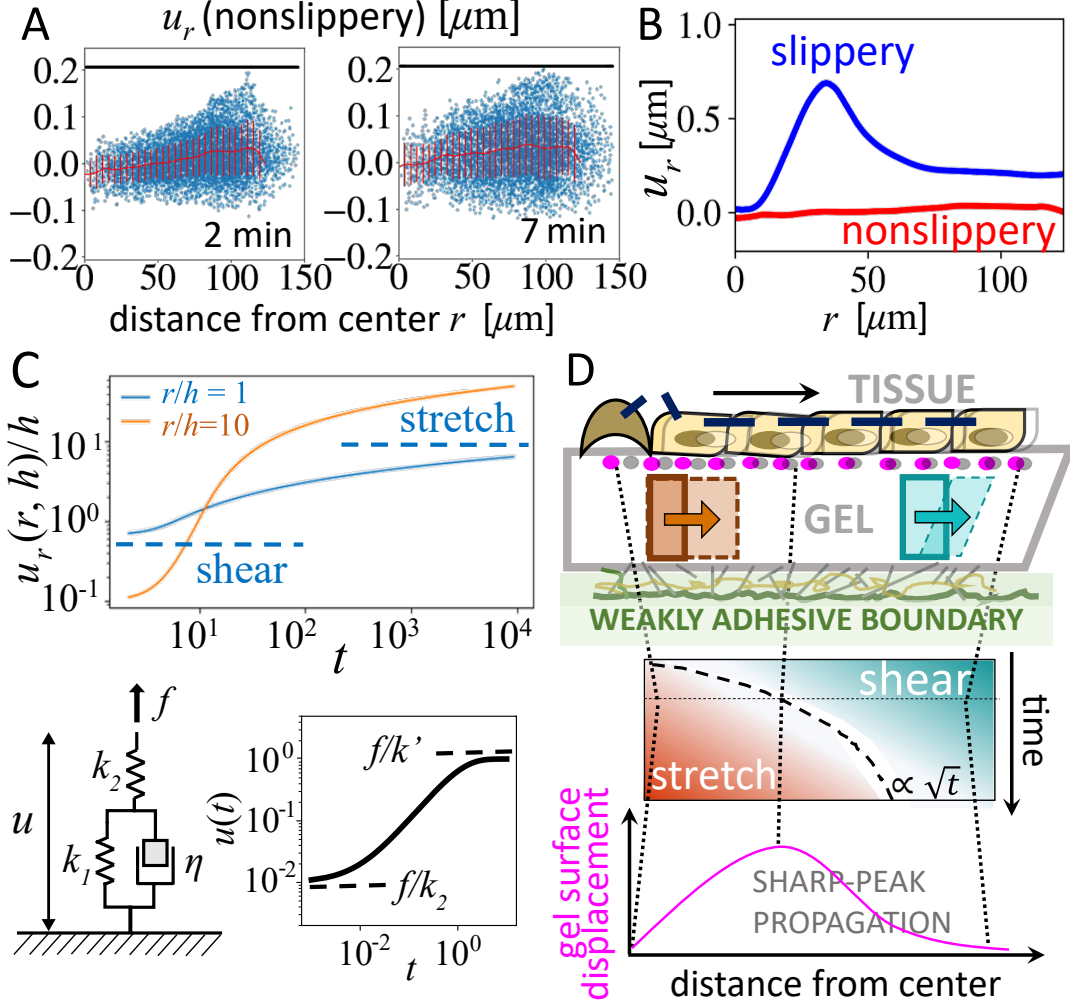


FIG. 4. Illustration of the physics underlying the deformation propagation in substrate. (A) Absence of propagation with a strongly adhesive (nonslippery) base of gel in experiment. Black line indicates the resolution threshold at $0.206\mu\text{m}$. (B) A comparison between the two typical samples under slippery (blue) and non-slippery (red) boundary conditions. (C) Top: “Creeping” dynamics of effective strain u_r/h (normalized by $s\varepsilon/\hat{G}$) at the gel surface for near field (blue curve) and far field (orange curve). Bottom: Creeping curve of a type of viscoelasticity model (Zener model) described in the schematic illustration. f represents the external stress, k_1 and k_2 mean two different parts of elastic modulus, η is the viscosity. Time evolution of the deformation u is given by $u(t) = (f/k_1)[1 - \exp(-t/\tau)] + f/k_2$ with $\tau = \eta/k_1$. Effective modulus $k' = 1/(1/k_1 + 1/k_2)$. For the graph, the parameters are set $f = 1$, $k_1 = 1$, $\eta = 1$ (units) and $k_2 = 100$. (D) Pedagogical picture of propagation. The mechanism of propagation in an elastic substrate lies in the expansion of the regime dominated by bulk stretching mode from the center ($r = 0$) over time. With a spatially decaying form of surface stress $S(r, t)$, the gel displacement peaks at the boundary between the stretch- and the shear-dominated regions. The Kymograph at the middle is reminiscent of that in Fig.1(C), where the stretching region coincides with an inward movement of beads; we have shown in theory that this coincidence might originate from a slow decrease with time in the stress exerted by the tissue, coupled with the stretching mode in the gel.

SUPPLEMENTARY INFORMATION

FULL THEORY AND THE DETAILED DERIVATION OF THE SOLUTION

In what follows, we assume that ν is asymptotically close to 1/2, i.e., an incompressible gel. Here, we start with the equations to determine the radial displacement field u_r , vertical displacement field u_z and pressure field P (Eqs. [4-6] of the main text), *i.e.*,

$$\frac{\partial^2 u_r}{\partial r^2} + \frac{1}{r} \frac{\partial u_r}{\partial r} - \frac{u_r}{r^2} + \frac{\partial^2 u_r}{\partial z^2} - \frac{2}{\hat{G}} \frac{\partial P}{\partial r} = 0, \quad (70)$$

$$\frac{\partial^2 u_z}{\partial r^2} + \frac{1}{r} \frac{\partial u_z}{\partial r} + \frac{\partial^2 u_z}{\partial z^2} - \frac{2}{\hat{G}} \frac{\partial P}{\partial z} = 0 \quad (71)$$

and

$$\frac{\partial^2 P}{\partial r^2} + \frac{1}{r} \frac{\partial P}{\partial r} + \frac{\partial^2 P}{\partial z^2} = 0, \quad (72)$$

respectively, where $\hat{G} = \frac{E}{1+\nu} = 2G$ is an effective shear modulus of the gel.

Note that u_r and u_z are not independent with each other due to the incompressibility condition

$$\nabla \cdot \hat{u} = \frac{1}{r} \frac{\partial}{\partial r} (r u_r) + \frac{\partial u_z}{\partial z} = 0. \quad (73)$$

Boundary conditions at the surface and top of the gel, $z = h$ and $z = 0$, are as follows:

$$\begin{cases} \sigma_{rz}|_{z=h} = S(r, t), \\ \sigma_{rz}|_{z=0} = \xi \frac{\partial u_r}{\partial t} \Big|_{z=0}, \\ \sigma_{zz}|_{z=h} = 0, \\ u_z(z=0) = 0, \end{cases} \quad (74)$$

where

$$\sigma_{rz} = \frac{\hat{G}}{2} \left(\frac{\partial u_r}{\partial z} + \frac{\partial u_z}{\partial r} \right) \quad (75)$$

is the shear stress, $S(r, t)$ is an unknown form of stress field exerted by the cells to the gel surface, named “surface stress”, and ξ is the friction coefficient that describes the force-velocity relationship at the bottom of the gel. As the other boundary conditions, we also assume the finiteness of $u_r(r \rightarrow 0)$, $P(r \rightarrow 0)$, $u_r(r \rightarrow \infty)$, and $P(r \rightarrow \infty)$.

To validate the zero external normal force boundary condition at the gel’s top surface, $\sigma_{zz}|_{z=h} = 0$, here we roughly compare the gel’s elastic normal stress $\sigma_{zz}|_{z=h}^{\text{el}} \sim E\epsilon_{zz} = E\delta h/h$ and tissue tension-originated one $\sigma_{zz}|_{z=h}^{\text{tt}} = \gamma\kappa = \gamma\nabla^2 h$ with the gel thickness $h \sim 50 \times 10^{-6}$ m, the gel’s elastic modulus $E \sim 10^4$ Pa (used in our experiment) and the tissue linear tension $\gamma = 10^{-3}$ N/m considering a 1 μm -thin belt of junctions [38, 44–46]. δh is the small change in the gel height as compared to the original gel height h , and $\kappa = \nabla^2 h$ is the curvature of the gel surface or the tissue layer, which could be approximated on the scale of cell size ℓ as $\delta_c h/\ell^2$, where $\delta_c h/\ell$ is the gradient of the surface height. One can see it obviously that $\delta_c h$ is smaller than δh in our problem when the gel is stretched in the radial direction due to the cell stress. Eventually, by approximating a typical cell length $\ell \sim 10^{-5}$ m, we can compare two normal stresses as $(\sigma_{zz}|_{z=h}^{\text{el}})/(\sigma_{zz}|_{z=h}^{\text{tt}}) = (E\ell^2)/(\gamma h) \times (\delta h/\delta_c h) \gtrsim 20 \gg 1$. This suggests that the normal stress due to the tissue tension $\sigma_{zz}|_{z=h}$ is negligible and the boundary condition $\sigma_{zz}|_{z=h} = 0$ is indeed valid.

We may solve Eqs. 72 and 70 by applying the method of separation of variable supposing $(1/u_r)\partial^2 u_r/\partial z^2 = k^2$ or $(1/P)\partial^2 P/\partial z^2 = k^2$ with an arbitrary constant k . The general solutions for the radial displacement field u_r and the rescaled pressure field $f \equiv 2P/\hat{G}$ to Eqs. 70 - 72 are given as

$$f(r, z) = \int_0^\infty dk J_0(kr) (C_k e^{kz} + D_k e^{-kz}) \quad (76)$$

and

$$u_r(r, z) = \int_0^\infty dk J_1(kr) \left[\left(A_k - \frac{C_k z}{2} \right) e^{kz} + \left(B_k + \frac{D_k z}{2} \right) e^{-kz} \right] \quad (77)$$

with the four coefficients A_k , B_k , C_k and D_k to be determined with the boundary conditions at $z = 0$ and h (Eq. 74) and Eq. 71. Here, J_1 is the Bessel function of first kind of order 1. To derive Eqs. 76 and 77, we have used the boundary conditions that $u_r(r \rightarrow 0)$, $u_r(r \rightarrow \infty)$, $P(r \rightarrow 0)$ and $P(r \rightarrow \infty)$ are finite. Using Eqs. 77 with the boundary conditions given in Eq. 74 and Eqs. 71 and 73, after a few manipulation, we obtain explicit forms of A_k , B_k , C_k and D_k and arrive at the solution

$$u_r(r, z, t) = \int_0^\infty dk J_1(kr) \left(Q(k, z) \mathcal{H}_1 \left\{ \frac{S(r, t)}{\hat{G}} \right\} - R(k, z) \mathcal{H}_1 \left\{ \frac{\xi}{\hat{G}} \frac{\partial u_r}{\partial t} \Big|_{z=0} \right\} \right) \quad (78)$$

with

$$Q(k, z) = \frac{\cosh(kh)\cosh(kz) - (kh)\sinh(kh)\cosh(kz) + (kz)\cosh(kh)\sinh(kz)}{\sinh(kh)\cosh(kh) + kh} \quad (79)$$

and

$$R(k, z) = \frac{\cosh(kh)\cosh(k(h-z)) - (kh)\sinh(kz) - (kz)\cosh(kh)\sinh(k(h-z)) + (kh)(k(h-z))\cosh(kz)}{\sinh(kh)\cosh(kh) + kh} \quad (80)$$

The notation \mathcal{H}_n means the Hankel transform of order n .

Transforming $u_r(r, z, t)$ by Hankel transform of order 1, we obtain $u_r(k, z, t)$ in wavenumber k -domain as:

$$u_r(k, z, t) = \frac{1}{k} Q(k, z) \tilde{S}(k, t) - \frac{\tilde{\xi}}{k} R(k, z) \frac{\partial u_r(k, 0, t)}{\partial t} \quad (81)$$

where $\tilde{S}(k, t) = S(k, t)/\hat{G}$ and $\tilde{\xi} = \xi/\hat{G}$. For $z = 0$, the solution to Eq. 81 is derived as

$$u_r(k, 0, t) = \frac{Q(k, 0)}{R(k, 0)} \frac{\tilde{S}(k, t)}{\tilde{\xi}} * M_0(k, t), \quad (82)$$

where M_0 is the memory kernel

$$\begin{aligned} M_0(k, t) &= \exp \left[-\frac{k}{\tilde{\xi} R(k, 0)} t \right] \Theta(t) \\ &= \exp \left[-\frac{k \sinh(kh)\cosh(kh) + kh}{\tilde{\xi} \cosh^2(kh) + (kh)^2} t \right] \Theta(t). \end{aligned} \quad (83)$$

Here, $*$ means the 1D convolution (the convolution over time) as introduced in the main text. Substituting $u_r(z = 0)$ given in Eq. 82 into Eq. 81, the final solution is

$$u_r(k, z, t) = S(k, t) * \left(m_s(k, z) \delta(t) + m_f(k, z) M_0(k, t) \right), \quad (84)$$

where

$$\begin{aligned} m_s(k, z) &= \frac{1}{\hat{G}} \frac{Q(k, z) R(k, 0) - Q(k, 0) R(k, z)}{k R(k, 0)} \\ &= \frac{1}{\hat{G} k} \frac{\cosh(kh)\sinh(kz) - (kh)\sinh(kh)\sinh(kz) + (kz)\cosh(kh)\cosh(kz) - (kh)(kz)\sinh(k(h-z))}{\cosh^2(kh) + (kh)^2} \end{aligned} \quad (85)$$

which is independent of friction, and

$$\begin{aligned} m_f(k, z) &= \frac{1}{\xi} \frac{Q(k, 0) R(k, z)}{R(k, 0)^2} \\ &= \frac{1}{\xi} \frac{\cosh(kh) - (kh)\sinh(kh)}{[\cosh^2(kh) + (kh)^2]^2} \left[\cosh(kh)\cosh(k(h-z)) \right. \\ &\quad \left. - (kh)\sinh(kz) - (kz)\cosh(kh)\sinh(k(h-z)) + (kh)(k(h-z))\cosh(kz) \right] \end{aligned} \quad (86)$$

which depends on friction. Fig.5(A) shows the z -dependency of u_r (normalized by $s\varepsilon/\hat{G}$ for a specific surface stress $S(r, t) = \Theta s\varepsilon/r$. The far field solution ($r > h$) does not vary too much with the increase of z ; yet the near field solution ($r < h$) increases with z . When $z = h$, a singularity appears because $u_r(r = 0)$ is not zero any more. This can be analytically seen from the derivations below.

At the surface $z = h$, Eqs 85 and 86 result in

$$m_s(k, h) = \frac{1}{\hat{G}k} \frac{\cosh(kh)\sinh(kh) + kh}{\cosh^2(kh) + (kh)^2} \quad (87)$$

and

$$m_f(k, h) = \frac{1}{\xi} \left[\frac{\cosh(kh) - (kh)\sinh(kh)}{\cosh^2(kh) + (kh)^2} \right]^2, \quad (88)$$

respectively. Moreover, z -averages of Eqs 85 and 86 from $z = 0$ to h , $\overline{m_{s/f}} \equiv (1/h) \int_0^h dz m_{s/f}(z)$, are given by

$$\overline{m_s}(k) = \frac{h}{\hat{G}} \frac{1}{\cosh^2(kh) + (kh)^2} \quad (89)$$

and

$$\overline{m_f}(k) = \frac{1}{\xi} \frac{\cosh^2(kh) - (kh)\sinh(kh)\cosh(kh)}{[\cosh^2(kh) + (kh)^2]^2}, \quad (90)$$

respectively.

SIMPLIFIED THEORY AND THE SOLUTION

Here we describe the details of the simplified theory. Instead of Eq. 70 we use

$$\frac{\partial^2 u_r}{\partial r^2} + \frac{1}{r} \frac{\partial u_r}{\partial r} - \frac{u_r}{r^2} + \frac{\partial^2 u_r}{\partial z^2} = 0, \quad (91)$$

where $\partial P/\partial r$ has been ignored. The boundary conditions are

$$\begin{cases} \sigma_{rz} \Big|_{z=h} = S(r, t) \\ \sigma_{rz} \Big|_{z=0} = \xi \frac{\partial u_r}{\partial t} \Big|_{z=0} \\ \frac{\partial u_z}{\partial r} \Big|_{z=0} = 0, \end{cases} \quad (92)$$

where σ_{rz} is given by Eq. 75. To complete the calculation, we also use the incompressible condition (Eq. 73).

Through the same method as that used in Section “FULL THEORY AND THE DETAILED DERIVATION OF THE SOLUTION” of SI, Eq. 91 leads to

$$u_r(r, z) = \int_0^\infty dk J_1(kr) (A_k e^{kz} + B_k e^{-kz}), \quad (93)$$

with only two integral coefficients A_k and B_k . Using the boundary conditions given in Eq. 92, we can determine A_k and B_k and eventually obtain Eq. 78 with

$$Q(k, z) = \frac{\cosh(kz)}{\sinh(kh)} \quad (94)$$

and

$$R(k, z) = \frac{2\cosh(k(h-z)) - \cosh(2kh)}{\sinh(kh)} \quad (95)$$

as the solution. Hence, by applying the same manipulations as those performed to derive the full solution in the previous section, we obtain Eq. 84 with the memory kernel

$$M_0(k, t) = \exp \left[-\frac{1}{\xi} \frac{k \sinh(kh)}{2 \cosh(kh) - 1} t \right] \Theta(t), \quad (96)$$

the friction-independent part

$$m_s(k, z) = \frac{1}{\hat{G}k} \frac{\sinh(kz)}{2 \cosh(kh) - 1} \quad (97)$$

and the friction-dependent part

$$m_f(k, z) = \frac{1}{\xi} \frac{2 \cosh(k(h-z)) - \cosh(kz)}{[2 \cosh(kh) - 1]^2}. \quad (98)$$

At the bottom $z = 0$, these results fall into

$$m_s(k, 0) = 0 \quad (99)$$

and

$$m_f(k, 0) = \frac{1}{\xi} \frac{1}{2 \cosh(kh) - 1}, \quad (100)$$

respectively. Moreover, taking z -averages from $z = 0$ to h , $\overline{m}_{s/f} \equiv (1/h) \int_0^h dz m_{s/f}(z)$, gives

$$\overline{m}_s(k) = \frac{1}{\hat{G}h} \frac{\cosh(kh) - 1}{k^2 [2 \cosh(kh) - 1]} \quad (101)$$

and

$$\overline{m}_f(k) = \frac{1}{\xi h} \frac{\sinh(kh)}{k [2 \cosh(kh) - 1]^2}, \quad (102)$$

respectively.

Figure 5(B-C) show the results of this simplified theory in the same format as that used for the full theory presentation (Fig. 3 of the main text), by which we can compare the results of the full theory and this simplified theory. As seen there, all the results of the simple theory (brown curves) differs from the full model (black curves) slightly in the near-center range (small r), yet the features of the peak propagation together with the $1/r$ decay in the far field are reproduced by the simplified model. This means that, for the mechanism giving rise to the peak propagation, the pressure inhomogeneity and the coupling between u_r and u_z are not important. The propagation of u_r itself is the essence of this single-peak wave propagation.

DYNAMIC SCALING OF THE MEMORY KERNEL $M(r, z, t)$

In this and the following sections, we provide the detail calculations on the most relevant solutions in a weakly adhesive (slippery) case and in a rigidly adhesive (nonslippery) case. In the calculations, integrals with Bessel functions are the key to the solutions and the technique of nondimensionalizing the variables is extensively used for deriving both rigorous and asymptotic solutions. In what may follow, friction between gel-glass interface is characterized by stress-velocity coefficient $\xi = \text{stress}/\text{velocity}$.

As demonstrated in the main text, $M(r, z, t)$ can be decomposed into two parts $M_s(r, z, t)$ and $M_f(r, z, t)$. The nature of diffusive propagation originates from the dynamic scaling of the friction dependent memory kernel $M_f(r, z, t)$ when the elapsed time t surpasses a critical scale $t_c = h\xi/\hat{G}$, i.e., the gel's thickness h is relatively small as compared with a critical length $t\hat{G}/\xi$ and z dependency becomes trivial. This is seen as follows:

The original friction-dependent kernel in k domain is:

$$M_f(k, z, t) = m_f(k, z) e^{-tk\hat{G}/(\xi R(k, 0))}, \quad (103)$$

where $R(k, 0)$ in full model is

$$R(k, 0) = \frac{\cosh^2(kh) + (kh)^2}{\sinh(kh)\cosh(kh) + kh}. \quad (104)$$

Substituting $\tilde{k} = kt\hat{G}/\xi$ into M_f , we then get:

$$M_f(\tilde{k}, z, t) = m_f(\tilde{k}, z)e^{-\tilde{k}/R(\tilde{k}\xi/\hat{G}t, 0)}. \quad (105)$$

When $t \gg t_c = h\xi/\hat{G}$, $\sinh(kh) \rightarrow kh$ and $\cosh(kh) \rightarrow 1$, thus the kernel keeps its time-dependency in the exponential terms in such a way:

$$M_f(\tilde{k}, z, t) = m_f(\tilde{k}, z)e^{-2\tilde{k}^2\xi h/\hat{G}t} \quad (106)$$

and consequently in r -domain:

$$M_f(r, z, t) = \int_0^\infty m_f(\tilde{k}, z)e^{-2\tilde{k}^2\xi h/\hat{G}t} J_1(kr) k dk. \quad (107)$$

Note that $m_f(\tilde{k}, z) = m_f(k, z, h \rightarrow 0) \sim 1/\xi$ when $t \gg t_c$ because the z -dependence becomes trivial.

Let $k' = \tilde{k}\sqrt{2\xi h/\hat{G}t} = k\sqrt{2\hat{G}th/\xi}$ and substitute into Eq. 107, we finally get

$$M_f(r, z, t) = \frac{\xi}{2\hat{G}ht} \int_0^\infty m_f(k', z)e^{-k'^2} J_1(k'r/r_c) k' dk', \quad (108)$$

and thus

$$M_f(r, z, t) = \frac{\xi}{2\hat{G}ht} \widetilde{M}_f\left(\frac{r}{r_c}, z\right), \quad (109)$$

where $r_c = \sqrt{2\hat{G}ht/\xi}$ and \widetilde{M}_f is the rescaled form

$$\widetilde{M}_f = \mathcal{H}_1^{-1}\{m_f(k, z, h \rightarrow 0)e^{-k^2}\}, \quad (110)$$

where the notation \mathcal{H}_1^{-1} means the Inverse Hankel transform of order 1. This spatial scaling $r_c \propto \sqrt{t}$ in M_f is the origin of a diffusive propagation in the final solution and if the surface stress field $S(r, t)$ decays in space as $S(r) \propto (1/r)^q$ ($0 < q < 2$), r_c is exactly where r_{peak} locates. This explains why the peak starts to propagate at $r \sim h$ (r_c only exists when $t > \xi/\hat{G}$, hence $r_c > h$).

PEAK MAGNITUDE IN 2D APPROXIMATION

As explained in the main text, when the elapsed time surpasses a critical scale $t_c = \xi h/\hat{G}$, the role of thickness of the gel is trivial and thus the solution for the z -averaged displacement \bar{u} can be representative for the 3D dynamics. With the surface stress $S(r, t) = s(\varepsilon/r)^q \Theta(r)\Theta(t)$, this solution is

$$\bar{u}_r = \frac{s}{2\pi} \left(\frac{\varepsilon}{r}\right)^q * * M_{2D}(r, t), \quad (111)$$

where “ $**$ ” is the 2D convolution over space, and the memory kernel M_{2D} is

$$M_{2D}(r, t) = \mathcal{H}^{-1}\left\{\frac{1 - e^{-2k^2t\hat{G}h/\xi}}{2k^2h\hat{G}}\right\}. \quad (112)$$

For sake of simplicity, $\Theta(t)$ is dropped in all the following calculations. The solution under 2D approximation ($h < \hat{G}t/\xi$) has a pronounced propagating peak, and the slope rising to the peak and the slope decaying from the

peak can be rigorously obtained by setting $t \rightarrow 0$ and $t \rightarrow \infty$. With $t \rightarrow 0$, M_{2D} is reduced to $\mathcal{H}^{-1}\{t/\xi\}$, then the solution is

$$\bar{u}_r(r, t \rightarrow 0) = \frac{st}{\xi} \left(\frac{\varepsilon}{r} \right)^q, \quad (113)$$

showing a decaying power the same as in the surface stress $S(r)$.

With $t \rightarrow \infty$, M_{2D} is reduced to $\mathcal{H}^{-1}\{1/k^2\}/(2h\hat{G})$, then the solution is

$$\bar{u}_r(r, t \rightarrow \infty) \propto r^{2-q}, \quad (114)$$

showing a rising power $2 - q$ if $0 < q < 2$.

The displacement field crosses over from $\bar{u}(r, t \rightarrow 0)$ to $\bar{u}(r, t \rightarrow \infty)$ in space and the turning point occurs at somewhere $r_c \propto \sqrt{t}$. Due to the nature of crossover, the magnitude of peak $u_{peak}(r = r_c)$ is not directly the intersection point of $\bar{u}_r(r, t \rightarrow 0)$ and $\bar{u}_r(r, t \rightarrow \infty)$. To calculate the peak magnitude, we need a rigorous inspection on the convolution Eq.111. As a simple demonstration, we calculate the case with $q = 1$ as follows.

The 2D convolution form can be represented as an integral with a Bessel function:

$$\bar{u}_r(r, t) = \frac{s\varepsilon}{\hat{G}} \int_0^\infty dk J_1(kr) \frac{1 - e^{-2k^2 t \hat{G} h / \xi}}{2k^2 h}. \quad (115)$$

By substituting $k' = k\sqrt{2t\hat{G}h/\xi} = kr_c$, which is a dimensionless wavenumber, into Eq.115, we get

$$\bar{u}_r(r, t) = \frac{s\varepsilon r_c}{2\hat{G}h} \int_0^\infty dk' J_1(k'r') \frac{1 - e^{-k'^2}}{k'^2}, \quad (116)$$

where $r' = r/r_c$ is a dimensionless radial distance. It is easily found that the integral in Eq. 116 peaks at $\tilde{r} = 1$ and the value of the peak is a constant

$$Z = \int_0^\infty dx J_1(x) \frac{1 - e^{-x^2}}{x^2} \sim 0.48227, \quad (117)$$

and finally the peak magnitude u_{peak} is found as

$$u_{peak} = Z \frac{s\varepsilon r_c}{2\hat{G}h} = Z s\varepsilon \sqrt{\frac{t}{2\hat{G}\xi h}}. \quad (118)$$

This skill of nondimensionalizing k in the integral is also valid for the calculations with q other than 1.

SOLUTION IN A NONSLIP LIMIT

In a nonslippery case, the friction $\xi \rightarrow \infty$, and the 2D approximation above is invalid. As explained in the main text, the friction-dependent kernel M_f would vanish and then the solution at the surface $z = h$ becomes

$$u_r^n(r, h, t) = \frac{S(r, t)}{2\pi} * * m_s(k, h) = \frac{s\varepsilon}{\hat{G}} \int_0^\infty dk J_1(kr) \frac{\sinh(kh)\cosh(kh) + kh}{k[\cosh^2(kh) + (kh)^2]} \quad (119)$$

with the surface stress $S(r, t) = s(\varepsilon/r)\Theta(r)\Theta(t)$.

By substituting k with $\tilde{k} = kh$, we get:

$$u^n(r, h) = \frac{s\varepsilon}{\hat{G}} \int_0^\infty d\tilde{k} J_1(\tilde{k}r/h) \frac{\sinh(\tilde{k})\cosh(\tilde{k}) + \tilde{k}}{\tilde{k}[\cosh^2(\tilde{k}) + \tilde{k}^2]}, \quad (120)$$

which is $\sim s\varepsilon/\hat{G}$ for $r < h$ and decays with $1/r$ for $r > h$ [Fig.6(A)].

ROLE OF SPATIAL ONSET OF SURFACE STRESS

Let's consider the surface stress $S(r, t) = S(r)\Theta(r - r_0)\Theta(t)$ ($r_0 > 0$). Substituting this stress field into the general convolution, we get the solution in 2D approximation for the slippery case as:

$$\bar{u}_r(r, t) = s\varepsilon \int_0^\infty kdk J_1(kr) J_0(kr_0) S(k) M_{2D}(k, t), \quad (121)$$

by comparing which with Eq. 115, we can see the only difference lies in the emergence of the factor $J_0(kr_0)$, which equals 1 when $r_0 = 0$.

By nondimensionalizing k , we can find that when $r_c > r_0$, i.e., $t > r_0^2\xi/\hat{G}$, the $J_0 \rightarrow 1$, so that we would get the same result with Eq. 115. Now remember 2D approximation $t > t_c$ is the condition for Eq.115 to be derived, and if the onset position r_0 is smaller than the gel thickness h (this is almost the case in all our experiments), the critical timescale (brought by nonzero r_0) $r_0^2\xi/\hat{G}$ is smaller than t_c . Hence the role of r_0 can be neglected in 2D approximation for a slippery case. Since the propagating dynamics in 3D has trivial dependency on the height of gel for $r > h$, any statement made with 2D approximation can hold for the propagation in 3D. In conclusion, the role of r_0 is trivial to the propagation of peak.

Similarly, we can understand the role of r_0 in a nonslip limit by substituting the surface stress with r_0 into Eq. 119 and arrive at:

$$u_r^n(r, h) = \frac{s\varepsilon}{\hat{G}} \int_0^\infty dk J_1(kr) J_0(kr_0) \frac{\sinh(kh)\cosh(kh) + kh}{k[\cosh^2(kh) + (kh)^2]}. \quad (122)$$

By nondimensionalizing k , we can find that for $r > r_0$, the J_0 factor is trivial so that the solution Eq.120 still holds. But for range $r < r_0$, the J_0 factor plays a role as shown in Fig.6(B). The deformation occurs most at where $r > r_0$ and $r < h$.

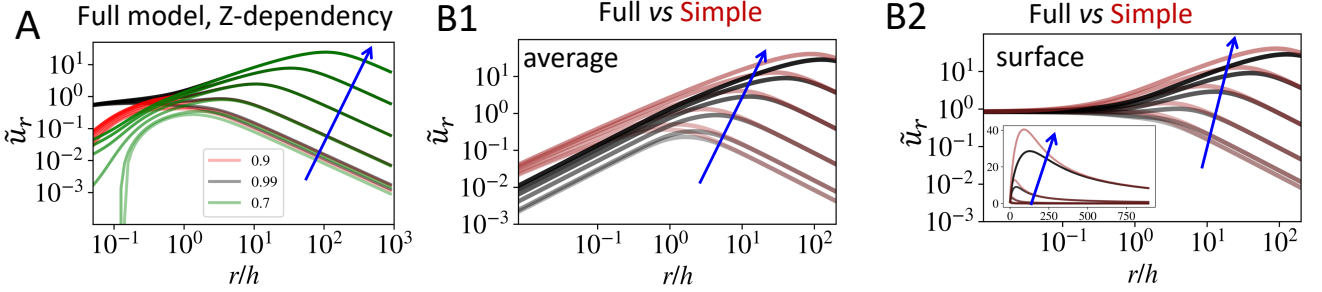
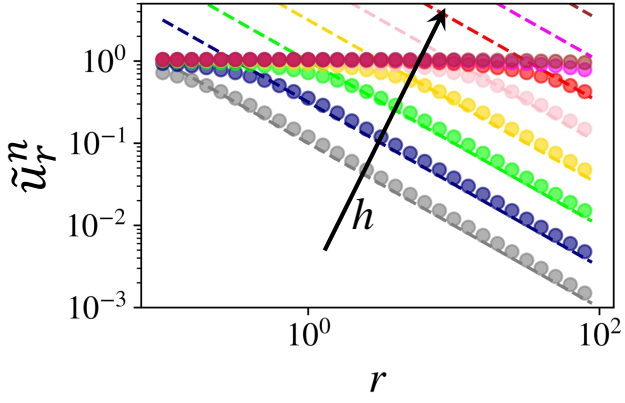


FIG. 5. Time evolution of radial displacement \tilde{u}_r , which is u_r normalized by $s\varepsilon/\hat{G}$, with the surface stress $S(r, t) = \Theta(t)s\varepsilon/r$. Blue arrows denote the time evolution. (A) The comparison between different height z with respect to h . (B) The comparison between the full model (black curves) and the simple model (brown curves). (B1) Solution averaged over z . (B2) Solution at surface $z = h$. The main figure is plotted in the log scale whereas the inset is in the linear scale.

A



B

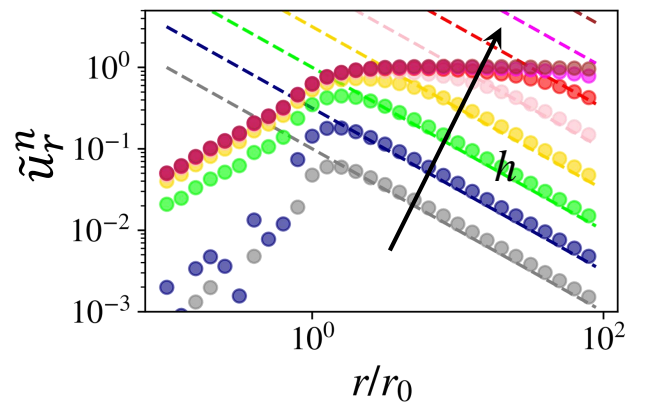


FIG. 6. The comparison of the nonslippery solution $\tilde{u}_r^n(r)$ (which is $u_r^n(r)$ normalized by $s\varepsilon/\hat{G}$) between (A) with $r_0 = 0$ and (B) $r_0 > 0$. Different colors represent different thickness h from 0.1 to 10^3 in (A) and from $0.1r_0$ to 10^3r_0 in (B).